J. Fluid Mech. (1986), *vol.* 168, *pp.* 255–289
Printed in Great Britain

Regimes of axisymmetric flow in an internally heated rotating fluid

By P. L. READ

Geophysical Fluid Dynamics Laboratory, Meteorological Office (21),
London Road, Bracknell, Berkshire RG12 2SZ, UK

(Received 5 July 1985 and in revised form 16 December 1985)

A boundary-layer scale analysis is presented for steady, zonally symmetric flow in a Cartesian channel of rectangular cross-section, subject to uniform internal heating, and cooling at the lateral boundaries, using an approach based on that of Hignett, Ibbetson & Killworth for a related system. Six main flow regimes are identified, depending chiefly upon the magnitude of the parameter P defined as the square of the ratio of the (non-rotating) thermal-boundary-layer thickness scale to that of the Ekman layers adjacent to the horizontal boundaries. For $P \ll A^{\frac{1}{6}}\epsilon^{\frac{1}{3}} (\gg 1$, where A is the Rayleigh number and ϵ the channel aspect ratio), the flow consists of an advectively dominated interior, characterized by a balance between vertical advection and internal heat generation, diffusively dominated thermal boundary layers adjacent to the sidewalls, and horizontal, viscously dominated Ekman layers (for non-zero rotation rate). If $P \ll 1$, the flow is only weakly modified by rotation, but as P increases through unity, rotation tends to inhibit heat transfer and thickens the thermal boundary layers. Provided $P \gg \epsilon^2\sigma^{-2}$, (where σ is the Prandtl number), the zonal flow is predominantly geostrophic, though not given by the conventional thermal-wind scale (based on the total thermal contrast ΔT) unless $P \gg 1$.

The results of the scale analysis are compared with laboratory measurements and numerical simulations of steady flow in a rotating, cylindrical annulus subject to (radially non-uniform) internal heating and sidewall cooling. Over the range of parameters accessible in the laboratory, the azimuthal velocity scale and thermal contrast were found to vary with rotation and heating rates in the way predicted from the scale analysis for the Cartesian system. Above a certain critical value of P (for the geometry used here $P_{\text{crit}} \approx 1$), the baroclinic wave regime was found to occur, corresponding to where rotational constraints first begin to influence significantly the heat transfer of the axisymmetric flow. The numerical simulations are compared with the laboratory measurements, and used to extend the ranges of rotation rate and aspect ratio over which the scale analysis could be verified. Good agreement was found for the dependence of globally averaged flow parameters on P, and the dynamical characteristics of each regime were further verified using explicit calculations of the balance of terms in the basic equations from the numerical model.

Further applications of the scaling technique to other, related systems are also discussed, together with a consideration of its generalization to systems of geophysical interest.

1. Introduction

Laboratory experiments on free thermal convection in a differentially heated rotating fluid annulus have, for many years, provided useful insight into studies of the circulations and flow instabilities in many systems of geophysical importance (e.g.

Hide 1953, 1958, 1969; Fultz *et al.* 1959; Fultz 1961; Hide & Mason 1975; Hart 1982). Most studies have concentrated upon the properties of baroclinic waves and eddies in a system heated and cooled at the side boundaries only, as representing the nearest analogue of the large-scale circulation and major energy-producing eddies in the terrestrial atmosphere and oceans. To establish the generality of conclusions derived from studies of such rotating baroclinic flows, however, it is desirable to investigate as many different configurations of basic temperature and motion fields and applied boundary conditions as possible.

If the heating and cooling is restricted to the boundaries of the system, the range of possible flow configurations is severely limited to ones in which heat is exchanged between the sidewalls via conductive boundary layers, and with a monotonically varying thermal gradient in a (largely adiabatic) interior. Hide & Mason (1970), however, suggested the use of internal heat sources, as well as at the boundaries, in order to extend the range of possible flows, and presented results on the flow patterns and heat transport when a fluid annulus is heated internally and cooled at one or both sidewalls. The conclusions suggested that, despite many variations in the appearance of the flow pattern, many key properties of the annulus waves do not depend strongly upon the form of differential heating employed, even when the horizontal thermal gradient is not monotonic – a conclusion largely supported in subsequent studies (e.g. Ukaji 1979; Read 1985, 1986*a*; White 1986).

A further motivation for studying the system cooled at both side boundaries has recently arisen from the suggestion (Hide 1980, 1981; Read & Hide 1983, 1984; Read 1986*b*) that the regular baroclinic eddies in such a system, with its non-monotonic horizontal thermal gradient, may be dynamically similar to the major long-lived oval eddies in the atmosphere of Jupiter and Saturn (including Jupiter's Great Red Spot and White Ovals). Detailed investigations of the dynamics of the corresponding laboratory system are particularly important in this context, in view of the profound implications of the latter suggestion for the stability of the atmospheric eddies, their role in the transport of heat, momentum and potential vorticity in the circulation of the atmospheres of the major planets, and the implied vertical and horizontal atmospheric structure (Read & Hide 1983, 1984; Read 1985, 1986*a*, *b*).

In all studies of thermally driven flows subject to axisymmetric forcing and boundary conditions, it is important to establish the dynamical characteristics and properties of the corresponding axisymmetric flow, since (*a*) an axially symmetric flow regime is actually observed in the laboratory (e.g. Hide 1969; Hide & Mason 1970, 1975); (*b*) a dynamically consistent, zonally symmetric flow is a necessary prerequisite for linear instability calculations; and (*c*) a knowledge of the properties of the corresponding axisymmetric flow may enable a quantification of the role of non-axisymmetric eddies in the circulation. Numerous investigations of axisymmetric flows in the boundary-heated annulus have appeared in recent years, including laboratory measurements (Bowden & Eden 1965; Kaiser 1971; Hignett 1982), numerical simulations (Williams 1967*a*, *b*) and various analytical studies (e.g. Hide 1967*a*, *b*; McIntyre 1968). Axisymmetric flows in the internally heated system, however, have been much less thoroughly studied, with previous laboratory studies limited to those of Hide & Mason (1970) and Ukaji (1979), together with the numerical and analytical study of Quon (1977). Most theoretical treatments of any of these systems have tended to concentrate upon one or two particular limiting cases, usually in regions of parameter space characterized by highly geostrophic flow in the interior, with few attempts at greater generality. The work of Quon (1977) represents the most detailed attempt so far to describe the internally heated flows analytically. By using

straightforward scaling techniques, he obtained estimates of the temperature contrast and its dependence on heating rate which compared favourably with his numerical simulations, although his analysis was subject to some *ad hoc* assumptions.

An approach which appears to offer the possibility of more general characterization of axisymmetric convection problems with rotation has recently been suggested by Hignett, Ibbetson & Killworth (1981, hereinafter referred to as HIK), in connection with their laboratory and analytical studies of rotating thermal convection driven by non-uniform heating along a horizontal surface. Their procedure involved a fully consistent scale analysis for the flow in the interior and major boundary layers, in which it was found that, over an extremely wide range of conditions, the properties of the flow depended mainly upon a suitably defined parameter (proportional to rotation rate Ω) measuring the ratio of the characteristic lengthscales of the two most significant boundary layers. By considering a contiguous sequence of limits for this parameter, all the main regimes of flow (defined in terms of the chief dynamical balances in the basic equations) obtainable in the system could be determined and located over the full range of rotation and imposed differential heating (subject to some minimal initial assumptions).

The present paper describes a further application of this approach to the internally heated/sidewall-cooled annulus, using a suitably modified form of the boundary-layer parameter of HIK. The scale analysis and its predictions for the properties of the various axisymmetric flow regimes are derived in §2 for a suitably defined Cartesian system analogous to the laboratory experiment. The following two sections then describe attempts to test and verify this analysis over a wide range of parameter space under realistic conditions. A series of laboratory measurements of horizontal velocity and temperature in an internally heated rotating annulus are presented in §3, indicating the properties of those axisymmetric flow regimes attainable in the annulus. In §4, these measurements are compared with, and extended by, numerical simulations of axisymmetric annulus flows subject to the same form of heating and boundary conditions, using a primitive-equation numerical model. By suppressing the development of non-axisymmetric instabilities, an axisymmetric flow could be sampled with the model over a wider range of parameter space than in the laboratory. More detailed diagnostics of the flow could also be obtained, thereby achieving a more rigorous test of the scale analysis, and also of the formulation and operation of the numerical model itself. The major conclusions are summarized and discussed in §5, with particular regard to further applications of the approach to other laboratory and geophysical systems.

2. Scale analysis and derivation of flow regimes

For simplicity, we choose to carry out the analysis for an incompressible Boussinesq liquid in Cartesian geometry. The results are then formally applicable to the flow in a rotating annulus of vanishingly small relative curvature, i.e. $2(b-a)/(b+a) \ll 1$, where a and b are the inner and outer radii of the annulus). We define a Boussinesq liquid as a fluid in which density variations are negligible except in the buoyancy term, and the coefficients ν, κ, and α (respectively of kinematic viscosity, thermal diffusivity and cubical expansion) may be regarded as constants. In ignoring curvature, we also take the centrifugal acceleration to be negligible compared with gravity (i.e. $\Omega^2 b/g \ll 1$, where Ω is the rotation rate and g is the gravitational acceleration). These assumptions are quite realistic except perhaps at the most rapid rotation rates considered (see §4.6 below).

2.1. *Basic equations and dimensionless parameters*

For incompressible two-dimensional flow (i.e. with no variation in the zonal direction y), it is convenient to define a meridional stream function ψ, such that

$$u = \psi_z, \quad w = -\psi_x, \tag{2.1}$$

where u and w are the lateral and vertical components of velocity, and the subscripts x and z denote partial differentiation in the lateral and vertical direction respectively. The steady, two-dimensional form of the Navier–Stokes and continuity equations can then be written as an equation for the specific zonal momentum

$$\nu\nabla^2 v = f\psi_z + J(v, \psi), \tag{2.2}$$

(where $f = 2\Omega$ and

$$J(c, d) = c_x d_z - c_z d_x, \tag{2.3}$$

in the conventional Jacobian notation), and a zonal vorticity equation

$$\nu\nabla^4\psi = g\alpha T_x - fv_z - J(\psi, \nabla^2\psi), \tag{2.4}$$

where T is the temperature and

$$\begin{aligned}\zeta &= u_z - w_x \\ &= \nabla^2\psi\end{aligned} \tag{2.5}$$

is the zonal component of vorticity. The thermodynamic equation becomes

$$\kappa\nabla^2 T + q + J(\psi, T) = 0, \tag{2.6}$$

where q represents the internal heating rate, obtained in the laboratory through ohmic dissipation produced by electrical heating (see §3 below and Hide and Mason 1970; Quon 1977). The boundary conditions to which the fluid is subject are

$$\psi = \psi_z = v = T_z = 0 \quad \text{on} \quad z = 0, H, \tag{2.7a}$$

$$\psi = \psi_x = v = T - T_0 = 0 \quad \text{on} \quad x = -\tfrac{1}{2}L, +\tfrac{1}{2}L, \tag{2.7b}$$

being an idealization of the laboratory configuration in which the fluid is contained by thermally insulating, rigid, non-slip endwalls at $z = 0$ and H, and isothermal ($T = T_0$), rigid, non-slip sidewalls at $x = -\frac{1}{2}L$ and $\frac{1}{2}L$. The problem may then be described in terms of five dimensionless parameters, viz. a Rayleigh number

$$A = \frac{g\alpha\Delta T L^3}{\kappa\nu} \tag{2.8}$$

(where ΔT represents the magnitude of the maximum temperature difference set up by internal heating), an Ekman number

$$E = \frac{\nu}{fH^2}, \tag{2.9}$$

the Prandtl number

$$\sigma = \frac{\nu}{\kappa}, \tag{2.10}$$

the meridional aspect ratio

$$\epsilon = \frac{H}{L}, \tag{2.11}$$

and a measure of the strength of the internal heating, defined here with respect to thermal conduction as

$$\mu = \frac{qL^2}{\kappa\Delta T}. \tag{2.12}$$

From (2.6), μ is seen to assume a significance for the internally heated system similar to the Nusselt number for the boundary-heated annulus, while $\mu-1$ may be viewed as a measure of the Péclet number (see §§2.2 and 3.2 below).

In the following scale analysis, the intention is to derive the dominant dynamical balances applicable to the interior and main boundary layers, and to obtain the dependence of internal parameters, such as ΔT and appropriate measures of v and ψ, on the external conditions (rotation and heating rates, and geometrical constraints), over as wide a range as possible. Accordingly, we restrict the initial assumptions as follows:

(i) the aspect ratio ϵ is not significantly different from unity;

(ii) there are single thickness scales, l for the side and h for the horizontal boundary layers;

(iii) outside the boundary layers there is a distinct interior flow characterized by horizontal lengthscale L and vertical lengthscale H, implying that $(l, h) \ll (L, H)$;

(iv) $\sigma \gg 1$.

Note that (ii) does not exclude other lengthscales, different in magnitude to l, which may be relevant to other passive boundary layers (i.e. which do not materially affect the most significant properties of the flow).

2.2. *The non-rotating problem*

To assist in the subsequent stages of the analysis, we first consider the problem without rotation, assuming the flow to consist of an advective interior and thin sidewall boundary layers (assumptions (ii) and (iii)). We non-dimensionalize (2.6) in the sidewall layer of thickness l, using

$$\left.\begin{aligned} \Delta x = l\Delta x_*, \quad \Delta z = H\Delta z_*, \quad q = \frac{\mu\kappa\Delta T}{L^2} q_*, \\ T - T_0 = \Delta T T_*, \quad \psi = \Psi\psi_*, \end{aligned}\right\} \tag{2.13}$$

where $(\,)_*$ denotes dimensionless variables of magnitude $O(1)$. Thus,

$$\nabla_*^2 T_* + \frac{\mu l^2}{L^2 q_*} + \frac{\Psi l}{\kappa H} J(\psi_*, T_*) = 0. \tag{2.14}$$

For an advective/diffusive balance, we require $\mu l^2/L^2 \ll 1$, hence implying that

$$\Psi = \frac{\kappa H}{l}. \tag{2.15}$$

For this case, the non-dimensional form of the vorticity equation (2.4) becomes, using (2.15),

$$\nabla_*^4 \psi_* = A\epsilon^{-1}\left(\frac{l}{L}\right)^4 (T_x)_* - \sigma^{-1} J(\psi_*, \nabla_*^2 \psi_*). \tag{2.16}$$

If $\sigma \gg 1$ (assumption (iv)), we obtain a buoyancy/viscous balance in the sidewall boundary layer, implying that

$$l = \epsilon^{\frac{1}{4}} A^{-\frac{1}{4}} L \,(= l_T) \tag{2.17}$$

(cf. Elder 1965; Gill 1966; McIntyre 1968 for the boundary-heated problem and Quon 1977 for internal heating), which is $\ll L$ provided that $A \gg \epsilon$. From (2.15), therefore,

$$\Psi = \kappa \epsilon^{\frac{1}{4}} A^{\frac{1}{4}}. \tag{2.18}$$

We now rescale (2.6) for the interior, using (2.13) and (2.18), but with $\Delta x = L\Delta x_*$; thus

$$\nabla_*^2 T_* + \begin{Bmatrix} \mu \\ \epsilon^2\mu \end{Bmatrix} q_* + \begin{Bmatrix} \epsilon^{-\frac{1}{4}}A^{\frac{1}{4}} \\ \epsilon^{\frac{1}{4}}A^{\frac{1}{4}} \end{Bmatrix} J(\psi_*, T_*) = 0, \tag{2.19}$$

where the terms in parentheses represent the cases $\epsilon \gtrless 1$. Provided that $\mu \gg \epsilon^{-2}$ and $A \gg \epsilon^{-7}$ (for $\epsilon < 1$), or $\mu \gg 1$ and $A \gg \epsilon$ (for $\epsilon > 1$), an internal heating/advection balance is found, implying that

$$\mu = O(\epsilon^{-\frac{1}{4}}A^{\frac{1}{4}}), \tag{2.20}$$

which is consistent with the assumption $\mu l^2/L^2 \ll 1$ provided that $A \gg \epsilon$. Hence, from (2.12),

$$\Delta T = q^{\frac{4}{5}}L\left\{\frac{\epsilon\sigma}{g\alpha\kappa^2}\right\}^{\frac{1}{5}}, \tag{2.21}$$

which is essentially the same result as found by Quon (1977) for his 'convective regime'.

2.3. *Effects of rotation*

We follow HIK and Hignett (1982) in noting that the thinnest horizontal boundary layer in a homogeneous rotating system is usually an Ekman layer of non-dimensional thickness $O(E^{\frac{1}{2}})$ (e.g. Fein 1978) when $E \ll 1$. We further anticipate that the ratio of the thicknesses of the sidewall thermal boundary layer (derived above) and the Ekman layer is of importance in describing the dynamics of the flow in the presence of rotation, and accordingly define a new dimensionless parameter

$$P = A^{-\frac{1}{2}}E^{-1}\epsilon^{-\frac{3}{2}}, \tag{2.22}$$

being the square of the ratio of the non-rotating value of l to the Ekman layer thickness (cf. Hignett 1982). This parameter then has the convenient property of being a linear function of rotation rate Ω, and accords a degree of physical insight into the meridional transport properties of the flow in a similar manner to the equivalent parameter Q discussed by HIK. If ΔT may be regarded as a measure of the vertical temperature contrast, it is also of interest to note that $P \sim \epsilon\sigma^{-\frac{1}{2}}L/(\text{Rossby radius})$, where the Rossby radius is given by $\bar{N}H/f$, $\bar{N}$ being the mean buoyancy frequency ($= [g\alpha\Delta T/H]^{\frac{1}{2}}$).

A possible disadvantage of this system of parameters, however, is that A and P both involve ΔT, and are therefore internal parameters, themselves determined by the flow. It is clearly desirable to define a set of external parameters which depend only upon those factors which would be under the control of an experimenter, namely the heating and rotation rates, q and Ω, geometry and fluid properties. Accordingly, we may define a further two parameters associated with P and A, thus,

$$\begin{aligned} A_c &= A\mu, \\ &= \frac{g\alpha q L^5}{\kappa^2\nu}, \end{aligned} \tag{2.23}$$

(cf. Carrigan 1985) and

$$\begin{aligned} P_c &= A_c^{-\frac{1}{2}}E^{-1}\epsilon^{-\frac{3}{2}}, \\ &= P\mu^{-\frac{1}{2}}, \end{aligned} \tag{2.24}$$

which are, respectively, the values of A and P obtained for a temperature scale defined by $\mu = 1$, so that $\Delta T = qL^2/\kappa$ (i.e. the 'conductive' temperature scale of Quon 1977 and below), and directly depend on the externally determined heating rate q.

A straightforward application of similar scaling analyses to those employed by HIK lead to the discrimination of six regimes for the system (although the number of definable regimes is somewhat arbitrary), the validity of which is found to depend mainly on the value of $\mathbb{P}$, and only weakly on the other parameters. Each regime, as defined below, corresponds to a different balance dominating in the governing equations for the interior and/or the principal boundary layers. The corresponding limits on $\mathbb{P}$ thus represent the formation of the Ekman layer as the dominant horizontal boundary layer (at $\mathbb{P} \approx \epsilon^2\sigma^{-2}$, see below), equal influence exerted by rotation and buoyancy at $\mathbb{P} \approx 1$, and the disappearance of a distinct sidewall thermal boundary layer at $\mathbb{P} = \mathbb{A}^{\frac{1}{4}}\epsilon^{\frac{1}{2}}$ (cf. the flow structure illustrated in figure 7 below). Following HIK for a fixed heating rate (and large $\mathbb{A}$) and assuming $\sigma \gg 1$, therefore, these six regimes can be written as:

(i) no rotation, $\mathbb{P} = 0$;
(ii) very weak rotation, $\mathbb{P} \ll \epsilon^2\sigma^{-2}$;
(iii) weak rotation, $\epsilon^2\sigma^{-2} \ll \mathbb{P} \ll 1$;
(iv) moderate rotation, $\mathbb{P} \approx 1$;
(v) strong rotation, $1 \ll \mathbb{P} \ll \mathbb{A}^{\frac{1}{4}}\epsilon^{\frac{1}{2}}$;
(vi) very strong rotation, $\mathbb{P} \gg \mathbb{A}^{\frac{1}{4}}\epsilon^{\frac{1}{2}}$;

and we briefly discuss their respective characteristics below.

(i) The non-rotating case has already been dealt with in §2.2 above, in which it was found that the flow is divided into an advective/internally heated interior in the thermodynamic equation, with sidewall boundary layers of thickness l_T (see (2.17)), characterized by the usual advective/diffusive balance. From a consideration of the interior balances in the zonal vorticity equation, we may estimate the magnitude of the isotherm slope ($\beta = \Delta T_h/\Delta T$, where ΔT_h is the horizontal temperature contrast across the interior). Provided σ is sufficiently large, a buoyancy/viscous balance operates, so that $g\alpha T_x (= O[g\alpha\Delta T\beta L^{-1}]) \approx \nu\nabla^4\psi (= O[\nu\Psi L^{-4}])$. Thus, $\beta \lesssim O(\epsilon^{\frac{3}{4}}\mathbb{A}^{-\frac{3}{4}}) \ll 1$.

The internal heating parameter μ is given by

$$\mu = O(\mathbb{A}_c^{\frac{1}{4}}\,\epsilon^{-\frac{1}{2}}) \gg 1, \tag{2.25}$$

in the external system (cf. (2.20)), and the value of ΔT implied (see (2.21)) is effectively an estimate of the vertical temperature contrast, and hence of the mean static stability in the interior. The advective term in (2.6) is then dominated by the contribution from wT_z, suggesting that motion in the interior is predominantly vertical and upwards for q and $T_z > 0$ except near the top and bottom boundaries. In the absence of rotation, (2.2) for v is decoupled from the other two basic equations, and motion occurs only in the meridional plane.

(ii) Increasing $\mathbb{P}$ from zero (but to less than $\epsilon^2\sigma^{-2}$) takes the system first into the very-weak-rotation regime. Since f is no longer zero, (2.2) is then coupled to (2.4) and the associated Coriolis torques render v non-zero. Because f is still very small in this regime, the scaling in the thermodynamic and vorticity equations remains as for (i), with the corresponding meridional transport properties, sidewall-boundary-layer thickness and scales for Ψ and μ unaffected by rotation. The latter presupposes, of course, that the sidewall thermal boundary layer is much thinner than any other boundary-layer scale (notably that of the Stewartson type, whose thickness l_S is $O(E^{\frac{1}{3}}H)$ in the present scheme, e.g. see Fein 1978). It is straightforward to show from the definition of l_T in (2.17) that this requires $\mathbb{P} \ll \mathbb{A}^{\frac{1}{4}}\epsilon^{\frac{3}{4}}$ for regime (ii), which is readily satisfied for $\epsilon^2\sigma^{-2} \ll 1$. To obtain an estimate for the zonal velocity scale V, we may scale (2.2) in the Ekman layer (assuming E is sufficiently small, though see §4.6 below) using

$$\Delta z = HE^{\frac{1}{3}}\Delta z_*, \quad \Delta v = V\Delta v_* \tag{2.26}$$

and (2.18) to obtain

$$\sigma\epsilon^{-1}\mathbb{P}^{\frac{1}{2}}\nabla_*^2 v_* = \frac{fL}{V}(\psi_z)_* + J(\psi_*, v_*). \tag{2.27}$$

The significance of the upper limit on $\mathbb{P}$ is now apparent since, for $\mathbb{P} \ll \epsilon^2\sigma^{-2}$, (2.27) is characterized by an advective/Coriolis balance in the Ekman layer. Outside the sidewall boundary layers (where an advective/viscous balance must operate in (2.2)), the entire flow is then characterized by local conservation of angular momentum (cf. the discussion of Read 1986*c*) with $V = O(fL)$ (i.e. proportional to $\mathbb{P}$). The scaling in the interior vorticity equation is therefore unchanged from (i), and the isotherm slope β remains $O(\epsilon^{\frac{3}{4}}\mathbb{A}^{-\frac{3}{4}}) \ll 1$.

(iii) As $\mathbb{P}$ increases beyond $\epsilon^2\sigma^{-2}$, the viscous term in (2.27) becomes the dominant term in the Ekman layer balancing the Coriolis term, thus rescaling V to $O(\kappa L^{-1}\mathbb{A}^{\frac{1}{2}}\epsilon^{\frac{1}{2}}\mathbb{P}^{\frac{1}{2}})$. This balance also extends into the interior, while in the sidewall boundary layers, the viscous/advective balance in the zonal momentum equation remains unchanged from (i). Despite the new scaling for V, the dominant balances in the thermodynamic equation remain unchanged (provided that l_T remains $\ll l_S$, and hence $\mathbb{P} \ll \mathbb{A}^{\frac{1}{4}}\epsilon^{\frac{3}{4}}$; see above), and the meridional heat transfer, μ and Ψ are still unaffected by rotation. The rescaling of V does affect the interior balance in the azimuthal vorticity equation, however, from a buoyancy/viscous to a buoyancy/Coriolis balance characteristic of geostrophic flow, even though V is not given by the usual 'thermal-wind' scale (cf. McIntyre 1968). The reason for this is that the isotherm slope in the interior now depends strongly on rotation ($\beta = O(\epsilon^{-1}\mathbb{P}^{\frac{3}{2}})$) in this regime (though it is still $\ll 1$), more than outweighing the $\mathbb{P}^{-1}$ dependence of the 'thermal wind' which would hold for constant β. The geostrophic character of the interior zonal flow may be further confirmed by forming the zonal Rossby number, defined as

$$\mathbb{R} = \frac{V}{fL}, \tag{2.28}$$

which, for this regime, is $O(\epsilon\sigma^{-1}\mathbb{P}^{-\frac{1}{2}})$ and therefore much less than unity.

(iv) In the intermediate regime, the Ekman-layer thickness becomes comparable with that of the sidewall boundary layer, and is therefore expected to begin to exert an influence upon the meridional circulation and the associated heat transfer. Anticipating that the zonal velocity scale for $\mathbb{P} \gg 1$ is the 'thermal-wind' scale (i.e. proportional to $\mathbb{P}^{-1}$, see below), we identify the region $\mathbb{P} = O(1)$ as the regime where $\partial V/\partial\mathbb{P} \approx 0$, so that V reaches its maximum value $V_0 = O(\kappa L^{-1}\mathbb{A}^{\frac{1}{2}}\epsilon^{\frac{1}{2}})$ extrapolated from regime (iii). Given that the Ekman layer now exercises the dominant influence upon the meridional circulation, we now assume that Ψ is rescaled to $O(V_0 H\mathbb{E}^{\frac{1}{2}}) = O(\kappa\epsilon^{\frac{3}{4}}\mathbb{A}^{\frac{1}{4}}\mathbb{P}^{-\frac{1}{2}})$. The latter scalings imply a slow broadening of the sidewall thermal boundary layer with $\mathbb{P}$ to $l'_T = O(l_T\mathbb{P}^{\frac{1}{2}})$ (where l_T is given by (2.17)), obtained by seeking an advective/diffusive balance for the thermodynamic equation in a sidewall boundary layer scaled on l'_T (cf. the discussion of §2.2). These scalings for V and Ψ also imply a weak rotational influence on the efficiency of heat transfer. Provided $l'_T \ll l_S$ (now requiring $\mathbb{P} \ll \mathbb{A}^{\frac{1}{10}}\epsilon^{\frac{3}{10}} \gg 1$), the thermal layer remains the dominant sidewall boundary layer, and μ is then modified to $O(\mathbb{A}^{\frac{1}{4}}\epsilon^{-\frac{1}{4}}\mathbb{P}^{-\frac{1}{2}})$, i.e. a slow decay with increasing rotation. The interior balance in the vorticity equation must remain geostrophic, but the isotherm slope β (still $O(\epsilon^{-1}\mathbb{P}^{\frac{3}{2}})$) is now of order unity so that ΔT_{h} begins to approach ΔT itself.

(v) As $\mathbb{P}$ is increased well beyond $\mathbb{P} = 1$, the Ekman layer becomes much thinner than the sidewall thermal boundary layer and effectively dominates the meridional

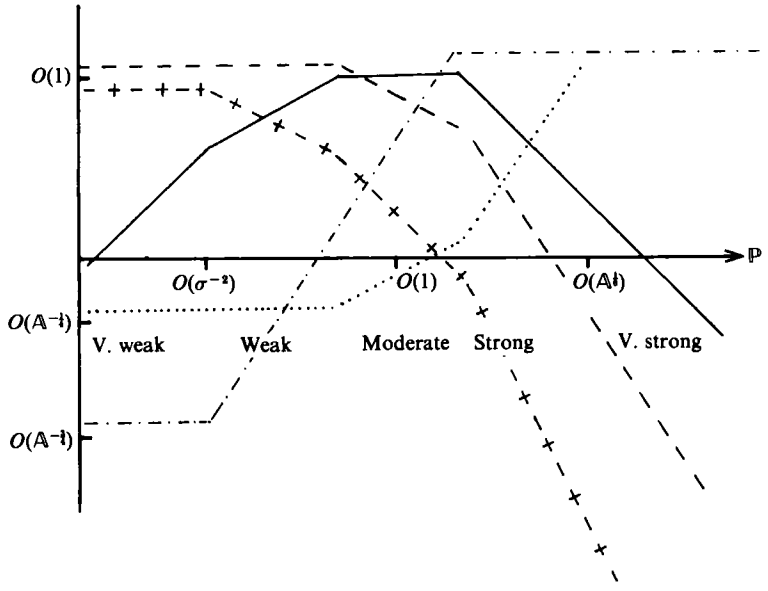

FIGURE 1. Schematic diagram showing the dependence of derived parameters on internal parameters in the various axisymmetric flow regimes defined in terms of $\mathcal{P}$ (assuming, for simplicity, that $\epsilon = 1$). Quantities represented are scaled as $VL/(\kappa A^{\frac{1}{4}})$ (——); $\Psi/(\kappa A^{\frac{1}{4}})$ and $\mu/A^{\frac{1}{4}}$ (– – –); $\beta = \Delta T_h/\Delta T$ (– · – · –); l/L (· · · · · ·); and $R = V/(fL)$ (– + – + –).

circulation, so that Ψ must remain $O(VHE^{\frac{1}{2}})$. As a result of the new scaling for Ψ, and the requirement for a geostrophic balance in the interior vorticity equation, the interior horizontal thermal contrast becomes static at $\beta = O(1)$ (i.e. $\Delta T_h \approx \Delta T$), and V is rescaled to the familiar 'thermal-wind' scale $V = O(\kappa A^{\frac{1}{2}} L^{-1} \epsilon^{\frac{3}{2}} \mathcal{P}^{-1})$. The (diffusive/advective) sidewall thermal boundary layer can accommodate these changes by expanding its thickness to $l_T'' = A^{-\frac{1}{4}} \epsilon^{-\frac{3}{4}} \mathcal{P}^{\frac{3}{2}} L$, thus extending the influence of thermal diffusion further into the interior. Provided that l_T'' remains $\ll L$, however, an internal-heating/advection balance in the thermodynamic equation can continue to operate in the interior and μ is rescaled to $O(A^{\frac{1}{4}} \epsilon^{\frac{3}{4}} \mathcal{P}^{-\frac{3}{2}})$, which is still $\gg 1$ (cf. the 'high-Péclet-number regime' of Hide 1967*a*, *b* and Hide & Mason 1975 for the boundary-heated annulus). Note that, since the Ekman layer now controls the meridional circulation, l_T'' can exceed l_S without affecting the overall transport properties of the flow.

(iv) At the most-rapid rotation rates, the expansion of the diffusive sidewall boundary layers extends their influence throughout the domain. The limit on $\mathcal{P}$ that discriminates between regimes (v) and (vi) may be seen, therefore, as expressing the requirement that $l_T'' = L$, which yields $\mathcal{P} = A^{\frac{1}{3}} \epsilon^{\frac{1}{2}}$. No separate advective interior for the thermodynamic equation exists in regime (vi), and μ is therefore $O(1)$ (although strictly $(\mu - 1) = O(A^{\frac{1}{4}} \epsilon^{\frac{3}{4}} \mathcal{P}^{-\frac{3}{2}})$ as before), implying that

$$\Delta T = O\left(\frac{qL^2}{\kappa}\right). \tag{2.29}$$

The internal and external parameters are therefore equivalent in this regime, so that V is now given by the 'thermal-wind' scale in both systems of parameters. In this conductively dominated regime, the temperature field reduces to the solution of a

Regime	V	Ψ	μ	β	l	R
(i) Non-rotating ($P = 0$)	0	$\kappa\epsilon^{\frac{3}{4}}A^{\frac{1}{4}}$	$(A/\epsilon)^{\frac{1}{4}}$	$(\epsilon/A)^{\frac{3}{4}}$	$(\epsilon/A)^{\frac{1}{4}}L$	1*
(ii) Very weak rotation ($P \ll \epsilon^2\sigma^{-2}$)	fL	$\kappa\epsilon^{\frac{3}{4}}A^{\frac{1}{4}}$	$(A/\epsilon)^{\frac{1}{4}}$	$(\epsilon/A)^{\frac{3}{4}}$	$(\epsilon/A)^{\frac{1}{4}}L$	1
(iii) Weak rotation ($\epsilon^2\sigma^{-2} \ll P \ll 1$)	$\kappa L^{-1}(A\epsilon P)^{\frac{1}{2}}$	$\kappa\epsilon^{\frac{3}{4}}A^{\frac{1}{4}}$	$(A/\epsilon)^{\frac{1}{4}}$	$\epsilon^{-1}P^{\frac{3}{2}}$	$(\epsilon/A)^{\frac{1}{4}}L$	$\epsilon\sigma^{-1}P^{-\frac{1}{2}}$
(iv) Moderate rotation ($P \approx 1$)	$\kappa L^{-1}(A\epsilon)^{\frac{1}{2}}$	$\kappa\epsilon^{\frac{3}{4}}A^{\frac{1}{4}}P^{-\frac{1}{2}}$	$(A/\epsilon)^{\frac{1}{4}}P^{-\frac{1}{2}}$	$\epsilon^{-1}P^{\frac{3}{2}}$	$(\epsilon/A)^{\frac{1}{4}}P^{\frac{1}{2}}L$	$\epsilon\sigma^{-1}P^{-1}$
(v) Strong rotation ($1 \ll P \ll A^{\frac{1}{3}}\epsilon^{\frac{1}{3}}$)	$\kappa L^{-1}(A\epsilon^3)^{\frac{1}{4}}P^{-1}$	$\kappa\epsilon^{\frac{7}{4}}A^{\frac{1}{4}}P^{-\frac{3}{2}}$	$\epsilon^{\frac{3}{4}}A^{\frac{1}{4}}P^{-\frac{3}{2}}$	1	$\epsilon^{-\frac{3}{4}}A^{-\frac{1}{4}}P^{\frac{3}{2}}L$	$\epsilon^2\sigma^{-1}P^{-2}$
(vi) Very strong rotation ($P \gg A^{\frac{1}{3}}\epsilon^{\frac{1}{3}}$)	$\kappa L^{-1}(A\epsilon^3)^{\frac{1}{4}}P^{-1}$	$\kappa\epsilon^{\frac{7}{4}}A^{\frac{1}{4}}P^{-\frac{3}{2}}$	1	1	L	$\epsilon^2\sigma^{-1}P^{-2}$

* $\lim \Omega \to 0$.

TABLE 1. Dependence of flow quantities on internal parameters for each regime

Poisson equation obtained by linearizing (2.6), so that the isotherms become steadily more vertical as P continues to increase (cf. the 'low-Péclet-number regime' of Hide 1967*a*, *b* and the 'conductive regime' of Quon 1977).

The results of the above analysis, in terms of the dependence of μ, Ψ, l, β, V and R on P, are summarized schematically in figure 1 and table 1.

2.4. *Comparison with the analysis of Quon* (1977)

Various aspects of the analysis given above have many features in common with the more restricted treatment of Quon (1977), and indicate some inconsistencies in the assumptions invoked in the latter work. Quon's analysis applies to a similar Cartesian system to that analysed above (but only for $\epsilon = 1$), and discusses a 'conductive regime', which is essentially the same as our regime (vi). The heat transfer is then dominated by diffusion throughout the flow, implying a temperature scale given by (2.29) as above, and a geostrophic zonal flow in the interior characterized by the 'thermal-wind' scale.

His alternative limit (the 'convective regime'), however, contains features which the present work shows to be mutually incompatible. Quon's analysis of the heat transfer in this regime effectively parallels that given above for regimes (i)–(iii), in which he derives an internal-heating/vertical advective balance in the interior thermodynamic equation, and diffusively dominated sidewall boundary layers of thickness $l = O(A^{-\frac{1}{4}}L)$ (cf. (2.17)), with an implied temperature scale as given by (2.21). He goes on to conclude from his initial assumptions that v is geostrophic in the interior (with the thermal-wind balance in the interior vorticity equation, as in our regime (iii)), but then incorrectly assumes that V is given by the usual 'thermal-wind' scale. As discussed above for regime (iii), this scaling for V cannot be compatible with Quon's 'convective scale' (2.21), since the latter also implies a strong dependence of the interior isotherm slope on Ω which combines to give a scale for V proportional to $\Omega^{\frac{1}{2}}$.

The present analysis allows for these interdependent effects in a more self-consistent way, thus avoiding the pitfalls of Quon's less general approach, and permits us to examine the full range of parameters within the limitations posed by the initial assumptions listed in §§2.1 and 2.2. Thus, we see that, if V is given by the

	Laboratory experiments	Numerical simulations
Inner radius, a (cm)	4.10	4.0
Outer radius, b (cm)	10.2	10.0
Annulus depth, d (cm)	16.05 ($\epsilon = 2.63$)	16.0 ($\epsilon = 2.67$) 6.0 ($\epsilon = 1$) 2.5 ($\epsilon = 0.325$)
Rotation rate, Ω (s^{-1})	0.01–1.0	10^{-4}–12.0
Power input, p_0 (W)	0–350	100
Coefficient of cubical expansion, α (K^{-1})	$2.90 \pm 0.02 \times 10^{-4}$	3.15×10^{-4}
Kinematic viscosity, ν ($cm^2\ s^{-2}$)	$1.62 \pm 0.02 \times 10^{-2}$	1.20×10^{-2}
Thermal diffusivity, κ ($cm^2\ s^{-2}$)	$1.31 \pm 0.01 \times 10^{-3}$	1.31×10^{-3}
Mean density, ρ_0 (gm cm^{-3})	1.044 ± 0.001	1.043
Prandtl number, σ	12.4 ± 0.3	9.16
Conductive Rayleigh number, A_c	4.3×10^6–3.0×10^8	9.08×10^7

TABLE 2. Experimental parameters for laboratory experiments and numerical simulations

'thermal-wind' scale and the interior remains advectively dominated, we must be in regime (v). The thermal boundary layer thickness l must therefore be greater than $O(A^{-\frac{1}{4}}L)$ (possibly implying an element of 'boundary-layer entrainment' as discussed by Quon 1977, though see below), and the temperature scale ΔT becomes the rotationally dominated 'convective' scale

$$\Delta T = L\left\{\frac{q}{g\alpha\nu^{\frac{1}{2}}}\right\}^{\frac{1}{2}}(f\epsilon)^{\frac{3}{4}}, \tag{2.30}$$

which lies between the 'convective' and 'conductive' scales discussed by Quon (1977) and above for regimes (i) and (vi). In connection with the passive role for the Stewartson $E^{\frac{1}{3}}$ sidewall boundary layers, assumed above, it is of interest to note that Quon's parameter h, used to measure the degree of 'boundary-layer entrainment' at the sidewalls, is defined in the present system as $h = PA^{-\frac{1}{4}}$. It therefore measures the ratio $(l_T/l_S)^3$ (for $\epsilon = 1$), and is < 1 for most cases of practical interest.

3. Laboratory verification

In the previous section a self-consistent scale analysis has been described for axisymmetric, steady thermal convection in any rotating fluid system which is heated internally and cooled at the lateral boundaries (or, in principle, vice versa with internal cooling and sidewall heating, e.g. see Read & Hide 1983). The most satisfactory way of verifying such an analysis is clearly to perform a series of carefully controlled experiments in the laboratory on a real fluid system to which the analysis may be expected to apply, taking appropriate measurements for comparison with the analysis. The following sub-sections discuss a series of such experiments in an internally heated, rotating, cylindrical annulus.

3.1. *Experimental configuration*

The experimental arrangement was similar in many respects to that used by Hide & Mason (1970) and Ukaji (1979), and the dimensions and other salient details of the apparatus are summarized in table 2 and illustrated in figures 2 and 3. The working fluid was contained in a cylindrical annulus of conventional design, with vertical,

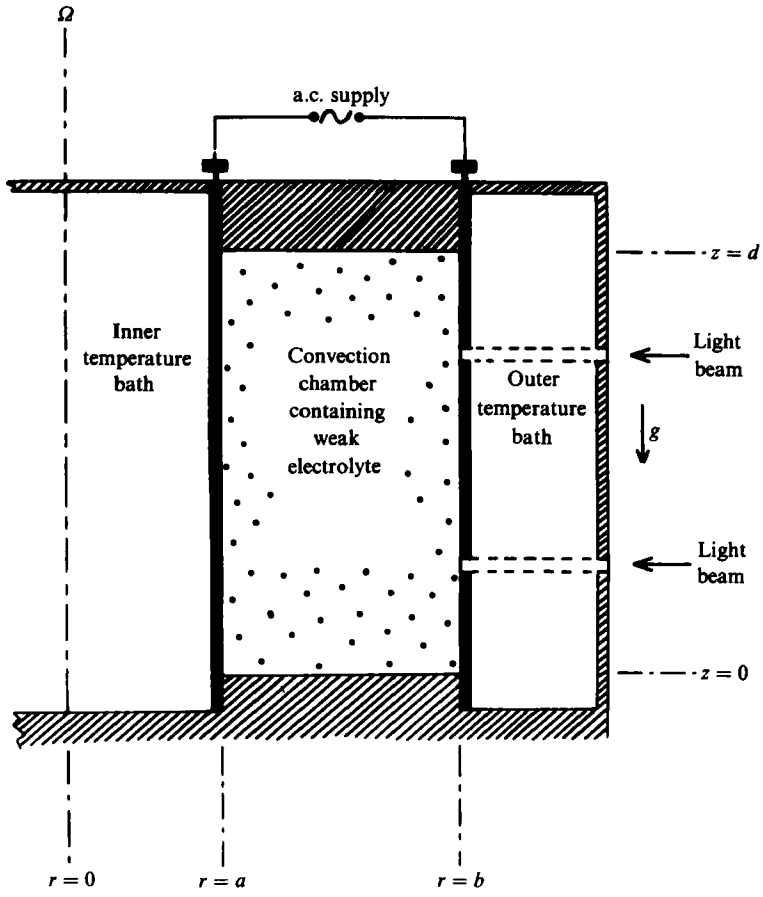

FIGURE 2. Schematic cross-section of the cylindrical annulus used for measurements of horizontal velocity and temperature in flows driven by internal heating. The convection chamber is viewed from above, and illuminated by narrow, horizontal beams of light at $z = 0.2d$ and $z = 0.7d$.

coaxial, thermally conducting (brass) sidewalls of thickness 5 mm at $r = a$ and 2.5 mm at $r = b$, and horizontal endwalls which were nominally thermally insulating (Perspex) at $z = 0$ and d. Unlike Hide & Mason (1970) and Ukaji (1979), however, the upper surface of the fluid was in contact with the rigid lid of the apparatus for all the experiments described herein.

The annulus was levelled (to within 10^{-4} rad) and centred on a turntable, driven by a servo-controlled, permanent-magnet d.c. motor. Long-term stability of the rotation rate (over periods of several hours, comparable with the duration of a typical run) was found to lie within one part in 10^3 between 0.1–1 rad s^{-1}. Short-term stability (over a small number of rotation periods) varied between one part in 10^4 at 1 rad s^{-1} and one part in 10^3 at 0.1 rad s^{-1}. The rotation rate could be conveniently varied between 10^{-2} and 5 rad s^{-1}.

The inside surface of the inner sidewall and the outside surface of the outer sidewall were both in contact with water baths, through which water at a carefully controlled temperature could be circulated at flow rates up to 8 l min^{-1}. To minimize vertical and azimuthal thermal gradients along each sidewall, the coolant water was injected into the water bath near the top of the convection chamber in an azimuthally swirling

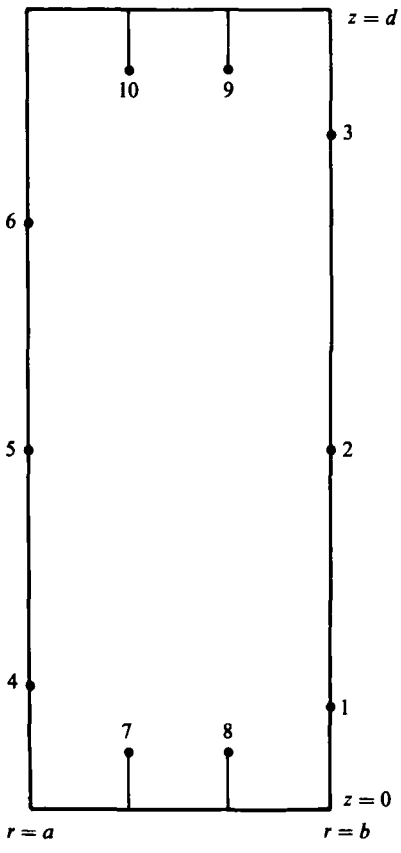

FIGURE 3. Schematic cross-section of the cylindrical annulus, indicating the positions of thermocouples 1–10 in a meridional slice.

flow (outer sidewall only), and withdrawn near the base of the apparatus. By this means, the wall temperatures were maintained constant to within 0.01 K, and with vertical gradients along the sidewalls limited to $< 0.05\ \Delta T_{\max}/d$ at the inner wall and $< 0.11\ \Delta T_{\max}/d$ at the outer wall.

The working fluid was heated in the same way as by Hide & Mason (1970), by passing an alternating electric current through the fluid (which was a weak electrolyte) using the two sidewalls themselves as electrodes (see figure 2). The magnitude of the heating rate could then be determined from measurements of the r.m.s. voltage applied to the sidewalls (typically up to 300 V) and the current passing through the fluid, and could be varied over the approximate range 0–350 W. The choice of working fluid was then partly dictated by the need to use a weak electrolyte, and also by the flow-visualization technique employed (see below). The fluid used was a mixture of glycerol and water (approximately 15% glycerol by volume), rendered weakly electrically conducting by the addition of a small quantity of an inorganic salt (usually $CuNO_3$). As discussed by Hide & Mason (1970) and Quon (1977), if the temperature variation of fluid properties is ignored, this form of electrical heating generates an internal (ohmic) heat source whose spatial form is

$$q/\mathrm{Ks}^{-1} = \frac{p_0}{2\pi \ln(b/a)\, d\rho_0 c_p r^2}, \tag{3.1}$$

where p_0 is the electrical power input (in Watts), ρ_0 the mean density and c_p the specific heat capacity of the fluid. In the absence of advective heat transfer, the resulting conductive temperature field is characterized by vertical isotherms, and a local maximum in temperature at the geometric mean radius $(ab)^{\frac{1}{2}}$, and equal partitioning of the heat flux removed at both sidewalls (i.e. precisely half the heat generated internally is withdrawn at each sidewall) if $T_a = T_b$.

Temperatures were measured using an array of copper–constantan thermocouples (sensitivity $\approx 40\ \mu\text{V K}^{-1}$), distributed in an azimuthal slice as shown in figure 3. Three thermocouples were sealed with epoxy resin into small holes in each sidewall in order to determine the thermal boundary condition acting on the fluid. The temperature distribution in the fluid itself was sampled by four more thermocouples in short, electrically insulated rigid probes, extending 1.2 cm into the convection chamber from the base and lid. All ten thermocouples were referenced to a further thermocouple maintained at 0 °C, and their voltages measured using d.c. amplifiers and a digital voltmeter, with an effective resolution of 1 μV.

Flow visualization was obtained using a suspension of polystyrene beads of diameter 600 μm, which were rendered nominally neutrally buoyant by adjusting the density of the working fluid (by altering the proportion of glycerol) until most of the beads were uniformly dispersed throughout the fluid at the anticipated mean operating temperature (cf. Hignett *et al.* 1985). The outer sidewall and water bath were made in three sections, between which were placed transparent acrylic inserts of thickness 5 mm (see figure 2) to enable the working fluid to be illuminated by a flat, horizontal beam of light at either of two levels in the vertical. The light scattered from the suspended beads was viewed through the transparent Perspex lid by a monochrome television camera mounted axially on the turntable. The horizontal trajectories of the beads (which were assumed to follow the motion of the fluid itself) could then be followed electronically using the automatic particle-tracking technique described by Jackson (1984) and Hignett *et al.* (1985).

The latter method makes use of the spatial and temporal coordinate systems of the television camera itself (suitably calibrated with respect to the frame of the apparatus) to measure the displacements of particles in successive raster scans of the image by the camera during preset time intervals. The data are then stored in a PDP 11/34 minicomputer. The time interval was chosen to give maximum particle tracks of 2–4 cm, and by this means, a series of scans of the two levels could be quickly obtained, each of which typically contained 150–400 randomly distributed velocity measurements. Subsequent processing analysed the radial and azimuthal velocity fields at each level using an interpolation scheme similar to that of Jonas & Kent (1979), to obtain a continuous analytical representation as an azimuthal Fourier series, the coefficients of which are expressed as a polynomial in the radial coordinate.

3.2. *Measurements and dimensionless parameters*

The facilities offered by the laboratory apparatus described in §3.1 enable measurements of the temperature difference and horizontal velocity fields to be obtained over a wide range of heating and rotation rates. For comparison with the scale analysis in §2, therefore, we define two measured parameters intended to represent the temperature scale set up by the internal heating,

$$\Delta T_{\text{m}} = \max(T_9, T_{10}) - \min(T_i) \quad (i = 1, 6), \tag{3.2}$$

(where T_i is the temperature at thermocouple i, see figure 3) and a measure of the

azimuthal velocity scale

$$V_{\mathrm{m}} = \left\{ \int_a^b (\bar{v}_1 - \bar{v}_2)^2 \, \mathrm{d}r/(b-a) \right\}^{\frac{1}{2}}, \tag{3.3}$$

at a given heating and rotation rate. The velocities $\bar{v}_1$ and $\bar{v}_2$ represent the azimuthally averaged components of v at the two illuminated levels in the fluid, and their radial dependence can readily be determined from the polynomial coefficients of the wavenumber $m = 0$ component of the azimuthal Fourier series analysed for v from the velocity measurements. To reduce random experimental errors in V_{m}, and to obtain estimates of their magnitude, five pairs of scans were used for each measurement (typically comprising a total of 2000–4000 individual particle trajectories), and the results combined to obtain a mean value and its standard deviation. By this means, measurements of V_{m} with formal uncertainties of 2–10% (typically 5%) were obtained over a range in velocity scale $0.01 < V_{\mathrm{m}} < 1$ cm s^{-1}.

Dimensionless measures of ΔT_{m} and V_{m} may also be defined as representing estimates of the corresponding parameters used in the scale analysis in §2. Thus, we obtain an internal Rayleigh number

$$A_{\mathrm{m}} = \frac{g\bar{\alpha}\,\Delta T_{\mathrm{m}}\, L^3}{\bar{\kappa}\bar{\nu}} \tag{3.4}$$

(where $\bar{\alpha}$, $\bar{\kappa}$, and $\bar{\nu}$ are the values appropriate to the mean temperature of the working fluid and $L = (b-a)$), an Ekman number based on $\bar{\nu}$ and $H = d$, and an internal boundary-layer parameter

$$P_{\mathrm{m}} = A_{\mathrm{m}}^{-\frac{1}{2}} E^{-1} \epsilon^{-\frac{3}{2}} \tag{3.5}$$

(cf. (2.22)), where $\epsilon = d/(b-a)$ as above. The parameter equivalent to μ needs to be defined carefully, taking the various geometrical factors into account (since the Cartesian analysis in §2 did not explicitly allow for spatial variations in q), so that $\mu = 1$ if heat transfer occurs by thermal conduction only. In this case, it is straightforward to show that, for isothermal, cylindrical sidewalls and perfectly insulating endwalls, ΔT reaches a maximum value at $r = (ab)^{\frac{1}{2}}$ of ΔT_{c}, where

$$\Delta T_{\mathrm{c}} = \frac{\lambda}{(2\bar{\kappa})} \{\tfrac{1}{4}[\ln(ab)]^2 - \ln(a)\ln(b)\}, \tag{3.6}$$

where

$$\lambda = \frac{p_0}{2\pi \ln(b/a)\, d\rho_0 c_p}, \tag{3.7}$$

(cf. (2.29), and Hide & Mason 1970; Quon 1977). A parameter with the required properties analogous to μ is therefore

$$\mu_{\mathrm{m}} = \frac{\Delta T_{\mathrm{c}}}{\Delta T_{\mathrm{m}}}, \tag{3.8}$$

which effectively differs from the 'Nusselt number' of Hide & Mason (1970) by a geometrical factor only.

The errors associated with the measurement of heat transfer, especially in a system primarily designed for visual observations, are well known (e.g. see Hide & Mason 1970, 1975; Hignett 1982). Although the present method of measurement is more direct than that commonly used for boundary-heated systems, systematic errors are bound to occur owing to stray exchanges of heat between the working fluid and the apparatus environment. The use of fixed probes to measure the maximum temperature contrast may also result in errors related to rotation and heating rates if the form

of the temperature field changes so that the position of maximum temperature is not constant. For strongly advective flows, however, the rapid motion in the endwall boundary layers results in very little horizontal temperature contrast in the vicinity of the Ekman layers themselves, the flow adopting the character of an internal jet (e.g. see Read 1985). Because the probes used in the present experiments only penetrated 1.2 cm into the interior from the horizontal boundaries, temperature differences between probes at the same level are therefore expected to be quite small, and were typically no more than $\approx 5\,\%$ of the maximum thermal contrast ΔT_{m}, suggesting that errors due to the latter effect ought to be negligible. Errors due to insufficient thermal insulation of the apparatus were minimized by carrying out most experiments at modest power inputs (so that ΔT was not too large) with a mean temperature close to that of the surrounding laboratory. It is estimated, therefore, that μ_{m} can be measured to an absolute precision of about $10\,\%$, although the repeatability of each measurement is typically within $3\,\%$, indicating the accuracy to which relative variations of μ_{m} can be measured.

In plotting the data, it is also useful to scale the dependent variables so that the values do not depend strongly on apparatus geometry or other physical properties of the system. Following the guidance from the scale analysis, therefore, we scale V_{m} by $\bar{\kappa}(\epsilon \mathcal{A}_{\mathrm{m}})^{\frac{1}{2}} L^{-1}$. In practice, it is found that μ_{m} is only ≈ 3–4, so that it is not strictly $\gg 1$. It is more appropriate, therefore, in comparing the results with the scale analysis, to form a measure of the Péclet number by subtracting the conductive component of μ_{m}, and to scale $(\mu_{\mathrm{m}} - 1)$ by the factors suggested from the scale analysis (cf. Hignett 1982 for measurements of Nusselt number in the boundary-heated annulus). Accordingly, $(\mu_{\mathrm{m}} - 1)$ is scaled by $(\mathcal{A}_{\mathrm{m}}/\epsilon)^{\frac{1}{4}}$.

3.3. *Results*

The results from a series of velocity and temperature measurements, carried out in an annulus for which $\epsilon = 2.63$, are shown in figure 4. The range in rotation rate covered is from ≈ 0.01 to nearly $1\ \mathrm{rad\ s^{-1}}$ at a nearly constant heating rate $p_0 \approx 100\ \mathrm{W}$ (corresponding to $\mathcal{A}_{\mathrm{c}} \approx 5.8 \times 10^7$). The range in $\mathcal{P}_{\mathrm{m}}$ covered by the experiments is limited at low rotation by practical difficulties in maintaining an even rotation rate and in measuring extremely slow velocities ($V_{\mathrm{m}} < 10^{-2}\ \mathrm{cm\ s^{-1}}$). At the upper limit of $\mathcal{P}_{\mathrm{m}}$ shown in figure 4, the range is limited by the onset of large-amplitude baroclinic waves, which occur for $\mathcal{P}_{\mathrm{m}} \gtrsim 1$ in the present system. The resultant flow is therefore highly non-axisymmetric beyond these limits, and the scale analysis described in §2 is no longer valid. As noted in §2.3, $\mathcal{P} \approx \sigma^{-\frac{1}{2}} \epsilon L f/(\bar{N} H) = \epsilon(\sigma \mathcal{B})^{-\frac{1}{2}}$, where $\mathcal{B}$ is the so-called Burger number (e.g. Gill 1982). Provided $\epsilon \sigma^{-\frac{1}{2}} = O(1)$, therefore, $\mathcal{P} \approx 1$ can be clearly associated with the principal stability criterion for baroclinic instability (e.g. see Hide & Mason 1975; Pedlosky 1979; Gill 1982). The parameter $\epsilon^2 \sigma^{-2} = 4.5 \times 10^{-2}$ for this series of experiments (indicated by B in figure 4), suggesting that axisymmetric regimes (ii)–(iv) may be just accessible.

Consistent with this interpretation, $(\mu_{\mathrm{m}} - 1)$ is found to be almost independent of $\mathcal{P}_{\mathrm{m}}$ (cf. table 1), apart from a weak (though statistically significant) decrease by about $10\,\%$ between the lowest and highest values of $\mathcal{P}_{\mathrm{m}}$. The decrease in $(\mu_{\mathrm{m}} - 1)$ is not sufficient to reach the $\mathcal{P}_{\mathrm{m}}^{-\frac{1}{2}}$ dependence suggested in §2 for regime (iv). At the lowest values of $\mathcal{P}_{\mathrm{m}}$, V_{m} is found to rise steeply with rotation rate, closely following the unity-exponent power-law dependence predicted for regime (ii). At the larger values of $\mathcal{P}_{\mathrm{m}}$, however, the gradient flattens off towards the $\mathcal{P}_{\mathrm{m}}^{\frac{1}{2}}$ dependence associated with regime (iii) (cf. table 1), apparently reaching a maximum at the onset of baroclinic waves around $\mathcal{P}_{\mathrm{m}} \approx 1$.

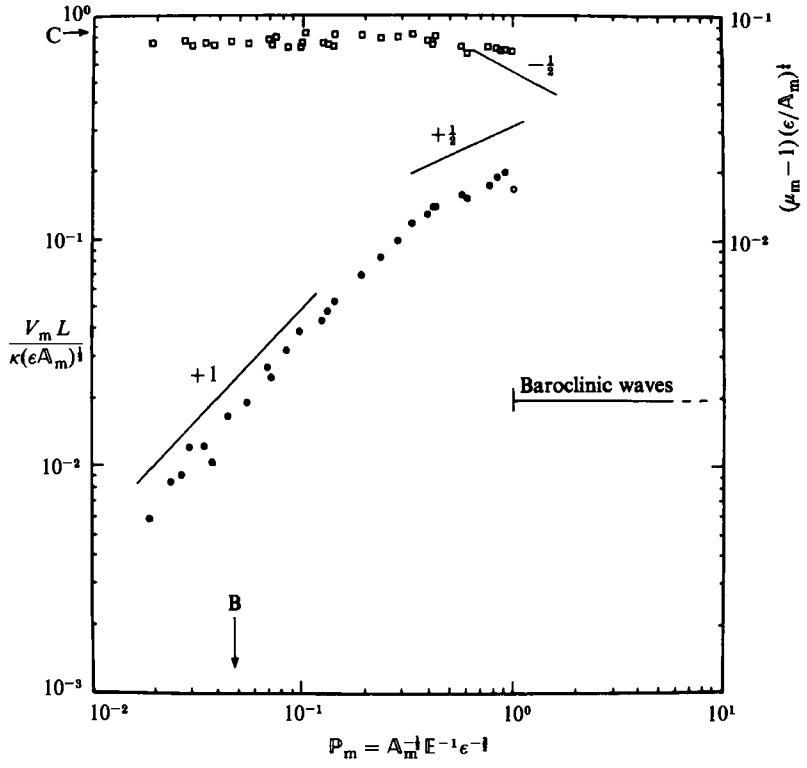

FIGURE 4. The variation of $(\mu_m - 1)$ and V_m, derived from measurements of horizontal velocity and temperature in the laboratory experiments described in §3, over a range of P_m obtained at a nearly constant value of $A_c (= 6 \times 10^7)$. Quantities plotted are $(\mu_m - 1)(\epsilon/A_m)^{\frac{1}{2}}$ (□) and $V_m L/[\kappa(\epsilon A_m)^{\frac{1}{2}}]$ (●) with respect to P_m. The limit delineating regimes (ii) and (iii) (see table 1) is shown as B, and the value of $(\mu_m - 1)$ measured at $\Omega = 0$ is indicated as C.

The measurements in figure 4 are evidently consistent with the scale analysis over the range of P_m accessible in the laboratory (within which axisymmetric flows actually occur), which appears to be limited to regimes (ii) and (iii) and the transition region towards regime (iv). Regime (i) can, of course, be approached in the laboratory (though not strictly achieved because of the Earth's rotation) by not rotating the apparatus, at least for temperature measurements. The corresponding value of μ_m (indicated as C in figure 4) agrees with that obtained at the lowest values of P_m in figure 4 to within the experimental errors.

Having established that the axisymmetric flows obtainable in the laboratory all appear to lie in the weak-rotation regimes, a further experiment which can be carried out to verify the scale analysis is to measure the dependence of ΔT_m and μ_m on the heating rate at low values of P. Figure 5(*a*) shows the results of a series of measurements carried out at very slow rotation rates, over a range in heating rate $7 \lesssim p_0 \lesssim 350$ W, plotting $(\mu_m - 1)$ as a function of A_c. The points all lie close to a straight line, corresponding to a power-law dependence of $(\mu_m - 1)$ on A_c with an exponent of 0.214 ± 0.014 (fitted by linear regression), in excellent agreement with the anticipated $\frac{1}{5}$ exponent predicted from the scale analysis (cf. (2.25)). As discussed in §2, this scaling for μ_m corresponds to a temperature scale given by (2.21) (assuming $\mu \gg 1$). Also plotted in figure 5(*b*), therefore, is the same data as in figure 5(*a*),

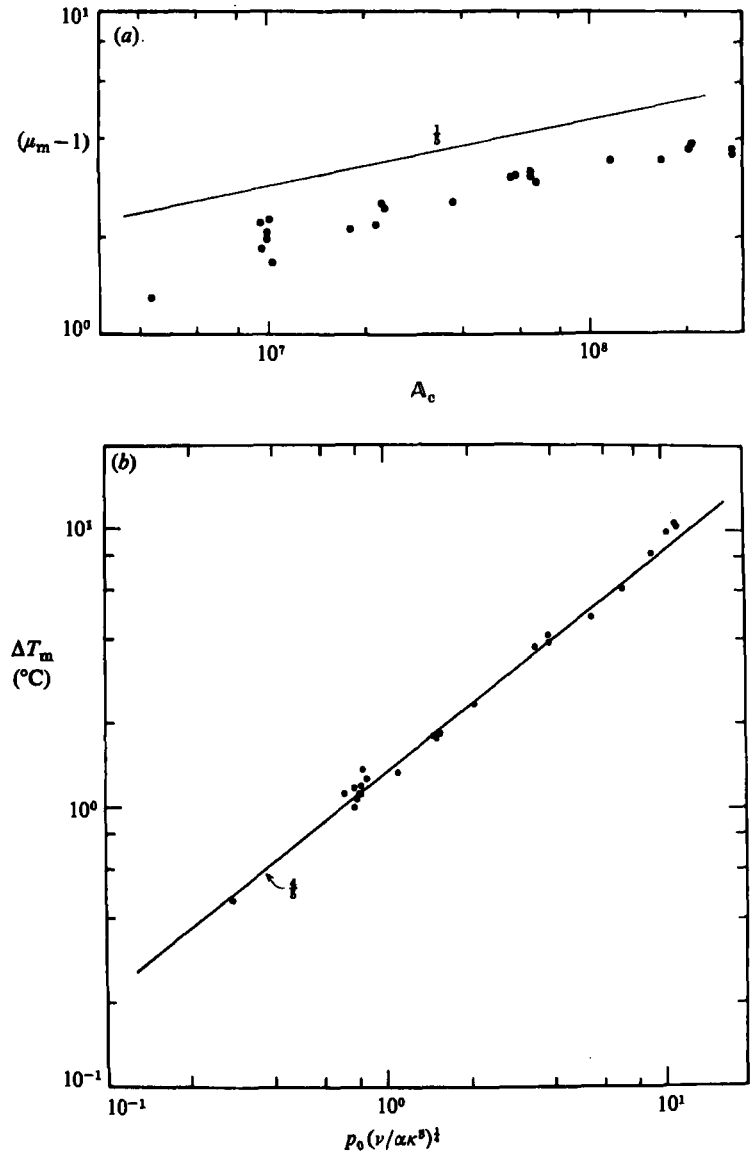

FIGURE 5. (*a*) The variation of $(\mu_m - 1)$ with $\mathbb{A}_c$ at low rotation rates (regimes (ii) and (iii)), obtained from measurements in the laboratory. The straight line indicates the $\frac{1}{5}$-exponent inferred from the scale analysis. (*b*) The variation of ΔT_m with power input p_0 (scaled according to (2.21)). The straight line indicates the $\frac{4}{5}$-exponent inferred from (2.21), assuming $\mu \gg 1$.

showing the variation of ΔT_m with p_0 (scaled by $(\bar{\alpha}/\bar{\nu})^{\frac{1}{3}}\bar{\kappa}^{\frac{2}{3}}$, as suggested from (2.21)). The results again lie close to a straight line, equivalent to an exponent of 0.85 ± 0.01, in less satisfactory agreement with the $\frac{4}{5}$ exponent suggested from (2.21). The discrepancy in agreement between the rigorously scaled plot of $(\mu_m - 1)/\mathbb{A}_c$ in figure 5 (*a*) and $\Delta T_m/p_0$ in figure 5 (*b*) may be seen as reflecting the fact that μ_m does not greatly exceed unity, and that the conductive component of heat transfer must therefore be taken into account.

3.4. *Discussion*

Within the range of P_m accessible for axisymmetric flows in the laboratory, therefore, measurements of parameters derived from the temperature and azimuthal velocity scales are found to be in good agreement with the scale analysis in §2.1 for their dependence on heating and rotation rates. The range over which the theoretical analysis has been tested is, however, quite limited, with at most three of the six regimes being amenable to full quantitative investigation. The onset of large-amplitude baroclinic waves prevents the axisymmetric regimes (iv)–(vi) being obtained in the laboratory, since their effects upon the flow (particularly with regard to heat transfer) cannot be neglected in comparison with the properties of the axisymmetric component of the flow. One way to overcome this limitation, at least in principle, would be to carry out another series of experiments in the 'lower-symmetric' region of the regime diagram (e.g. Hide & Mason 1970, 1975). This regime is only attained in the laboratory for extremely small temperature differences and heating rates, however, rendering accurate measurement of the temperature and velocity scales extremely difficult.

Hignett (1982) encountered similar difficulties while investigating the heat-transfer properties of axisymmetric flows in the boundary-heated annulus, but was able partly to overcome them by using sloping endwalls to suppress the development of the baroclinic waves, well into his equivalent of regimes (iv) and (v) (cf. Mason 1975). It remains to be seen whether this approach is feasible for the internally heated system, although it is likely that the configuration of sloping boundaries will need to be more complicated than for the boundary-heated system, owing to the non-monotonic form of the temperature field (see Hide & Mason 1970, 1975; Mason 1975; Quon 1977 and §4.3 below).

4. Numerical experiments

A further means of obtaining information on axisymmetric flows in a rotating annulus over a wide range of parameters, also discussed by Hignett (1982), is to obtain numerical simulations of the flow using a sufficiently realistic and well-formulated numerical model. Provided such a model is formulated with due regard to its formal accuracy and finite-difference schemes, and has sufficiently realistic geometry, fluid properties and boundary conditions, the simulations may be regarded in certain respects as an extension of the laboratory experiments. Furthermore, if the model is designed to exclude non-axisymmetric effects (by omitting terms in the equations of motion, continuity and thermodynamics which depend on azimuth angle θ), the development of instabilities and waves, such as the large-amplitude baroclinic waves found in §3, may be effectively suppressed in the resulting simulations. The possibility is therefore raised of using such a numerical model to explore the properties of a dynamically consistent axisymmetric flow in an otherwise realistic configuration at values of $P > 1$, thereby giving access to regimes (iv)–(vi) in addition to the other three regimes accessible in the laboratory.

4.1. *The numerical model*

The numerical model employed in the present study is a two-dimensional, axisymmetric version of the finite-difference Navier–Stokes model used by James, Jones & Farnell (1981), Hignett *et al.* (1985) and Read (1985, 1986*a*, *b*). This model integrates the time evolution of the non-hydrostatic equations of motion, continuity and

thermodynamics for an incompressible, Boussinesq liquid in cylindrical annular geometry. A reduced centrifugal term $\Omega^2 ri\alpha(T-T_0)$ (where i is a unit vector in the outward radial direction) is included in the momentum equation, thereby incorporating possible departures of the apparent vertical from the axis of symmetry and rotation. An equation of state

$$\rho = \rho_r[1-\alpha(T-T_r)] \tag{4.1}$$

is also assumed, where T_r and ρ_r are a reference temperature and density respectively. The pressure P is represented as the deviation from the reference function

$$P_r(r,z) = \rho_r g(d-z)+\tfrac{1}{2}\rho_r \Omega^2 r \tag{4.2}$$

and the internal heat source q in the thermodynamic equation is as given in (3.1) (i.e. as used by Quon 1977).

The model employs a finite-difference scheme similar to that of Williams (1969, 1972) with a typical resolution of 16×16 or 16×32 points respectively in r and z. A stretched mesh is used, however, to enhance the resolution of the model in the boundary layers (cf. Quon 1977) by applying a hyperbolic tangent rule for the grid spacing, with a lengthscale related to a notional boundary-layer thickness δ (i.e. the Ekman-layer depth $(\nu/\Omega)^{\frac{1}{2}}$ on horizontal boundaries, and the smaller of Stewartson ($E^{\frac{1}{3}}H$) and thermal ($A^{-\frac{1}{4}}L$) boundary-layer thicknesses at the sides – see Hignett *et al.* 1985 for further details). The finite-difference schemes are formally accurate to second order on the non-uniform grid. The advection terms in the momentum equation are represented by a modified form of the scheme of Piacsek & Williams (1970) to ensure consistency of the kinetic-energy budget, while in the thermodynamic equation, the advection term is represented in flux form (Arakawa 1966) so as to conserve total temperature. Time integration uses the leap-frog scheme, with Du Fort–Frankel representation of the diffusion terms (see James *et al.* 1981; Hignett *et al.* 1985). The timestep required was found to depend upon the rotation rate, with 0.1 s being an adequate compromise between computational economy and numerical stability for the lowest-rotation-rate experiments, but rather shorter timesteps (as short as 0.01 s in some cases) were required for $\Omega > 2$ rad s^{-1}. The pressure field is determined diagnostically at each timestep from the solution of a Poisson equation (see James *et al.* 1981; Hignett *et al.* 1985) using the method of Farnell (1980), applying the condition that the normal pressure gradient vanish at the boundaries.

The boundary conditions applied were intended to represent the conditions pertaining to laboratory experiments, such as those in §3, with a rigid lid in contact with the top surface of the fluid. The conditions applied were therefore similar to those used by Williams (1967*b*), thus

$$u = v = w = (T-T_a) = 0 \quad \text{at} \quad r = a, b, \tag{4.3a}$$

$$u = v = w = T_z = 0 \quad \text{at} \quad z = 0, d. \tag{4.3b}$$

In a typical experiment, the flow was initialized by an isothermal ($T = T_a$) state at rest in a frame rotating at the required value of Ω. The heating was then applied and the model run with the boundary conditions (4.3*a*, *b*) until a steady state was reached, usually requiring 2000–5000 s of simulated time to reach equilibrium.

4.2. *Dimensionless parameters*

To test the predictions of the scale analysis for the global properties of the flow in a similar manner to the laboratory experiments of §3, we need to define suitable measures of the temperature and zonal velocity scale from the model fields. For the

temperature scale, it is straightforward to obtain the maximum value of $\Delta T'$ set up by the internal heating,

$$\Delta T_{\mathrm{n}} = \max\,(T - T_0), \tag{4.4}$$

In the final steady-state temperature field. For the azimuthal velocity scale, it was convenient to make use of the volume-averaged zonal kinetic energy, calculated routinely at intervals during each experiment. The azimuthal velocity scale for the numerical simulations is therefore defined as

$$V_{\mathrm{n}} = \left\{\int_0^d \int_a^b v^2 r\,\mathrm{d}r\,\mathrm{d}z \Big/ \int_0^d \int_a^b r\,\mathrm{d}r\,\mathrm{d}z\right\}^{\frac{1}{2}}. \tag{4.5}$$

Dimensionless measures of ΔT_{n} and V_{n} can again be defined for comparison with those given in §3.2 (although they will inevitably differ quantitatively by small amounts due to differences of definition). Thus, $\mathcal{A}_{\mathrm{n}}$, $\mathcal{P}_{\mathrm{n}}$ and μ_{n} are given by (3.4)–(3.8) using ΔT_{n} as defined in (4.4), while V_{n} is scaled by $\kappa L^{-1}(\epsilon \mathcal{A}_{\mathrm{n}})^{\frac{1}{2}}$.

4.3. *Results for global parameters*

The first series of experiments consists of a number of numerical simulations in an annulus of similar dimensions to the laboratory system discussed in §3 (with $\epsilon = 2.67$), in which the heating rate was maintained at a constant value $p_0 = 100$ W and the flow simulated over a wide range of rotation rate. Figure 6 shows the variation of the suitably scaled values of $(\mu_{\mathrm{n}} - 1)$ and V_{n} over a range in Ω from 10^{-4} to 12 rad s^{-1}, illustrating their behaviour with respect to the internal parameters. The limiting values of $\mathcal{P}_{\mathrm{n}}$ for the regimes discussed in §2 (see table 1) are indicated in figure 6, and suggest that regimes (ii)–(v) are sampled in the present series of experiments.

As found for the laboratory experiments in §3, $(\mu_{\mathrm{n}} - 1)$ is virtually independent of $\mathcal{P}_{\mathrm{n}}$ at the lowest values of Ω, and only begins to decrease as $\mathcal{P}_{\mathrm{n}}$ approaches unity. The values of $(\mu_{\mathrm{n}} - 1)$ derived from the model, however, appear to decrease with $\mathcal{P}_{\mathrm{n}}$ somewhat more rapidly as $\mathcal{P}_{\mathrm{n}} \to 1$ than the corresponding laboratory results (cf. figures 3 and 5). The velocity scale V_{n} over this region varies as $\mathcal{P}_{\mathrm{n}}^{+1}$ at the lowest values of Ω, and more weakly with $\mathcal{P}_{\mathrm{n}}$ as $\mathcal{P}_{\mathrm{n}} \to 1$. It is of interest to note that V_{n} does not exhibit the slight kink around $\mathcal{P}_{\mathrm{n}} \approx 0.4$, as noted for the laboratory measurements. These observations may be indicative of some shortcomings in the numerical model as simulations of the laboratory flows, perhaps associated with the development of weak, non-axisymmetric baroclinic instabilities near the upper-symmetric transition (cf. Hide & Mason 1978; Jonas 1980), although such waves were not detected explicitly in the present experiments.

As suggested from the scale analysis, V_{n} reaches its maximum value around $\mathcal{P}_{\mathrm{n}} \approx 1$, while $(\mu_{\mathrm{n}} - 1)$ decays gradually with $\mathcal{P}_{\mathrm{n}}$ (cf. the line representing the power law $\mathcal{P}_{\mathrm{n}}^{-\frac{1}{2}}$ in figure 6) consistent with the properties derived for regime (iv). At increasing values of $\mathcal{P}_{\mathrm{n}}$, V_{n} turns over and begins to approach the $\mathcal{P}_{\mathrm{n}}^{-1}$ dependence at the highest values of Ω investigated. $(\mu_{\mathrm{n}} - 1)$ also continues to decrease more sharply with $\mathcal{P}_{\mathrm{n}}$, approaching (and possibly exceeding) the $\mathcal{P}_{\mathrm{n}}^{-\frac{3}{2}}$ dependence anticipated from the scale analysis for regime (v).

The behaviour of the model results are therefore, like the laboratory experiments, in reasonable agreement with expectations from the scale analysis, although the results suggest a rather ambiguous distinction between regimes (v) and (vi) at the aspect ratio of this configuration. This may be due to the relatively small difference between the limits 1 and $\mathcal{A}_{\mathrm{n}}^{\frac{1}{6}} \epsilon^{\frac{1}{2}}$ (a factor of $< 10^2$), so that the required limits for regime (v) are difficult to achieve satisfactorily. Conversely, it is possible that model

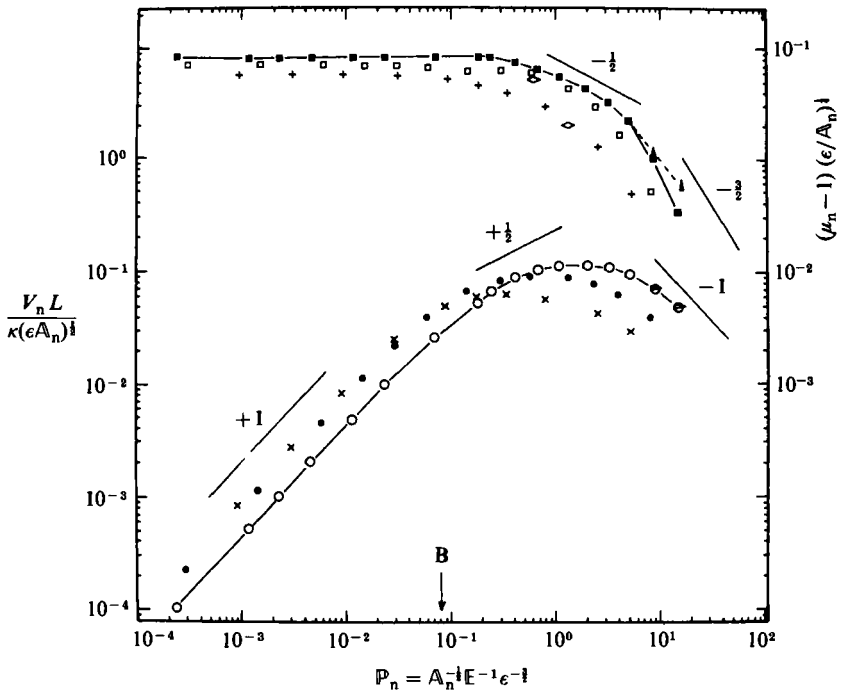

FIGURE 6. The variation of $(\mu_n - 1)$ and V_n, derived from numerical simulations of flow in an internally heated rotating annulus at three different aspect ratios for the same value of $\mathbb{A}_c (= 9.08 \times 10^7)$. Quantities plotted are $(\mu_n - 1)(\epsilon/\mathbb{A}_n)^{\frac{1}{2}}$ and $V_n L/[\kappa(\epsilon \mathbb{A}_n)^{\frac{1}{2}}]$ with respect to $\mathbb{P}_n$, and the different aspect-ratio results are denoted by $\epsilon = 2.67$ [■ and ○], $\epsilon = 1$ [□ and ●] and $\epsilon = 0.325$ [+ and ×]. Also shown are $(\mu_n - 1)$ for cases 3 and 4 of Quon (1977) (denoted by ◇). At higher values of $\mathbb{P}_n$ for $\epsilon = 2.67$, results are shown which were obtained with single-precision computations (denoted by △ joined by dashed lines for $(\mu_n - 1)$, and by ▷ for V_n) for comparison with the double-precision results (see text). The limit $\mathbb{P}_n = \epsilon^2 \sigma^{-2}$ delineating regimes (ii) and (iii) for $\epsilon = 2.67$ is indicated as B.

shortcomings have introduced systematic inaccuracies into the simulations. Results from early simulations, carried out in the region $\mathbb{P}_n \approx 10$ with single-precision (32-bit) computations, are shown in figure 6 as dashed lines for $(\mu_n - 1)$ and V_n, and indicate significant differences from the results obtained with double-precision (64-bit) arithmetic (joined by a continuous line in the same regions of figure 6). The difference between single- and double-precision simulations increases with $\mathbb{P}_n$ (with the results being virtually identical for $\mathbb{P}_n \lesssim 2$), suggesting a need to investigate further the effects of model precision in this region of parameter space. The effect of model resolution should also be investigated further, since the grid stretch is somewhat extreme for the largest values of $\mathbb{P}_n$ considered here. The latter factors may account for the sharper decrease of $(\mu_n - 1)$ with $\mathbb{P}_n$ in figure 6 than the $\mathbb{P}_n^{-\frac{3}{2}}$ suggested from the scale analysis for regime (v).

4.4. *Effects of different aspect ratios*

In comparing results from several different experiments, the role of the aspect ratio ϵ needs to be considered. The scale analysis in §2 suggested that the essential dynamics are not significantly affected by ϵ, provided that it is not too different from unity, and indicates an appropriate scaling of the various dimensionless parameters

to take account of different values of ϵ (see table 1). To invesigate the effects of different values of ϵ, the numerical experiments described above for $\epsilon = 2.67$ were supplemented by two further series of simulations at $\epsilon = 1$ and 0.325 (but at the same value of A_c), thereby spanning the full range over which most laboratory experiments are commonly carried out.

Figure 6 shows the results from all three series of experiments, plotted onto the same diagram. All three aspect-ratio series exhibit qualitatively the same behaviour, with $(\mu_n - 1)$ independent of P_n until $P_n \gtrsim 1$ and decaying with P_n thereafter, and with V_n also rising to a maximum just below $P_n \approx 1$. The scaling for μ_n, V_n, and P_n, designed around the expected behaviour of the flow at low rotation, maps all the results into fairly narrow regions of parameter space. Agreement between the various experiments is particularly close for μ_n and V_n at $P_n < 10^{-1}$. Systematic departures from a 'universal' behaviour, as represented by the present scaling, become evident at higher values of P_n. This is especially marked in the variation of V_n, and may be partly attributable to the dependence of the limits distinguishing the various axisymmetric regimes upon ϵ itself, particularly for the two weakly rotating regimes (ii) and (iii), which occur for $P_n \lesssim \epsilon^2 \sigma^{-2}$. The scale analysis also suggests a different overall dependence of μ_n and V_n on ϵ for the higher-rotation regimes (see table 1), so that we should not expect there to exist a single scaling which is universally valid for all values of P. Over the range of P_n accessible in the laboratory ($P_n \lesssim 1$), however, good agreement is found, and the scaling suggested by §2 is largely confirmed. This conclusion is in broad agreement with the work of Hignett (1982), who successfully combined heat-flow measurements in the boundary-heated annulus from a variety of laboratory and numerical sources with differing aspect ratios using essentially the same scaling for Nusselt number and P as given here.

For completeness, we also show some results for μ_n from the simulations of Quon (1977) in figure 6 (using the values of ΔT listed in his table 2). The range in P_n of Quon's experiments lies between $0.6 < P_n < 32$, so that the regimes sampled are more limited than in the present study (corresponding roughly to regimes (iv)–(vi)). The upper boundary condition also differs from the present work in being stress-free ($u_z = v_z = 0$) rather than non-slip (see (4.6*b*)). The results for his cases 3 and 4 are shown in figure 6, and both lie within the region of parameter space occupied by the present work, although $(\mu_n - 1)$ for the more weakly heated experiment (case 3) is systematically lower than for the other $\epsilon = 1$ results at comparable values of P_n. As in the boundary-heated annulus, the upper stress-free surface does not appear to affect strongly the radial heat transport (e.g. see Hignett 1982), which remains dominated by the properties of the Ekman layer adjacent to the lower, non-slip boundary. The other two cases discussed by Quon (1977) cannot be plotted in the present scheme since, according to Quon's table 2, the values of ΔT obtained from his numerical simulations actually exceed ΔT_c (so that $(\mu_n - 1) < 0$, cf. (3.8)). The latter result may indicate some shortcomings in the model used by Quon (1977), possibly related to the difficulties encountered with computational precision discussed above for the present model, especially since the temperature differences in his more weakly heated experiments are extremely small ($\Delta T \approx 5 \times 10^{-3}$ K). The numerical scheme for the thermodynamic equation in Quon's model was also formulated to conserve T^2 (see Quon 1976), in contrast to our model (see §4.1 above). The possibility that this difference in formulation could lead to errors of this type should also be investigated further.

4.5. *Fields of motion and temperature*

The form of the temperature and velocity fields in the various regimes is also of interest both from the viewpoint of the scale analysis in §2 and more generally. Figure 7 shows a series of examples of T-, v- and ψ-fields at values of $\mathcal{P}_n$ roughly representative of regimes (ii)–(v) for the experiments at $\epsilon = 1$.

The most striking variations are found in the form of the temperature field in figures 7(*a*), (*d*), (*g*) and (*j*). As suggested by the scale analysis, the slope β of the isotherms in the interior ranges from nearly zero (i.e. horizontal) in regime (ii) to $\beta \approx 1$ (nearly vertical) in regime (v), with $\beta \approx 0.7$ in figure 7(*g*) corresponding approximately to regime (iv). The sidewall-boundary-layer structure is also highly regime-dependent. The T-field in figure 7(*a*) (regime (ii)) is readily divided between a nearly isothermal interior and intense thermal boundary layers adjacent to each sidewall, the structure of which is nearly independent of height. There is some evidence of convective overshoot in the isotherm structure just outside the thermal boundary layer itself, characteristic of a buoyancy/viscous balance in a 'momentum' boundary layer whose thickness is significantly greater than $(A/\epsilon)^{-\frac{1}{4}}$ (cf. the similarity solution and associated discussion of McIntyre 1968 for the boundary-heated annulus, Mobbs 1986, and §4.6 below). The T-field in figure 7(*d*) (regime (iii)) still shows little variation in the boundary-layer structure with height, although the interior isotherms now show a perceptible slope, and the convective overshoot pattern is less obvious (although the contouring method employed may not show this structure very effectively). By regime (iv) (figure *g*), considerable vertical structure in the thermal boundary layers is evident, with the largest gradients concentrated near the upper corners of the annulus. The convective-overshoot pattern is no longer discernible, and the isotherms in the interior smoothly match into the boundary layers, with the reversal of the horizontal temperature gradient now clearly apparent around $r = (ab)^{\frac{1}{2}}$. The number of isotherm contours has also increased, indicative of the increasing value of ΔT_n as the Ekman layer begins to influence the efficiency of advective heat transfer in the flow. As anticipated from §2, by regime (v) (figure 7*j*), the thermal boundary layers are showing evidence of expansion into the interior, while the density of isotherms continues to increase rapidly as we enter the fully Ekman-dominated regime. As the isotherms in the interior become more vertical, it is clear that the flow is approaching the purely conductive solution as $\mathcal{P}_n$ increases towards regime (vi).

The azimuthal velocity fields show much less qualitative change in structure between the various regimes. Figure 7(*e*), (*h*) and (*k*) all exhibit a four-jet pattern, with anticyclonic horizontal shear in the interior at upper levels and cyclonic shear at lower levels. This presumably reflects the predominance of a geostrophic interior balance in the vorticity equation, deduced in §2 for regimes (iii)–(vi). Only figure 7(*b*) differs from this pattern, suggesting that the dynamics of this regime for v indeed differ from the other three illustrated in figure 7.

The meridional stream function, too, shows little qualitative variation with regime. The decrease in Ekman-layer thickness with increasing values of $\mathcal{P}_n$ is readily apparent in the ψ-fields illustrated in figure 7, with the horizontal motion occupying a large fraction of the annulus in regime (ii) (figure 7*c*) and only a tiny fraction of the depth in regime (v) (figure 7*h*). The increasing role of Proudman–Taylor constraints on w_z in the interior with increasing values of $\mathcal{P}_n$ (and Ω) is also evident, with the isolines of ψ becoming steadily more vertical in moving through regimes (ii)–(v). Despite the increasing thickness of the thermal boundary layers with $\mathcal{P}_n$, the

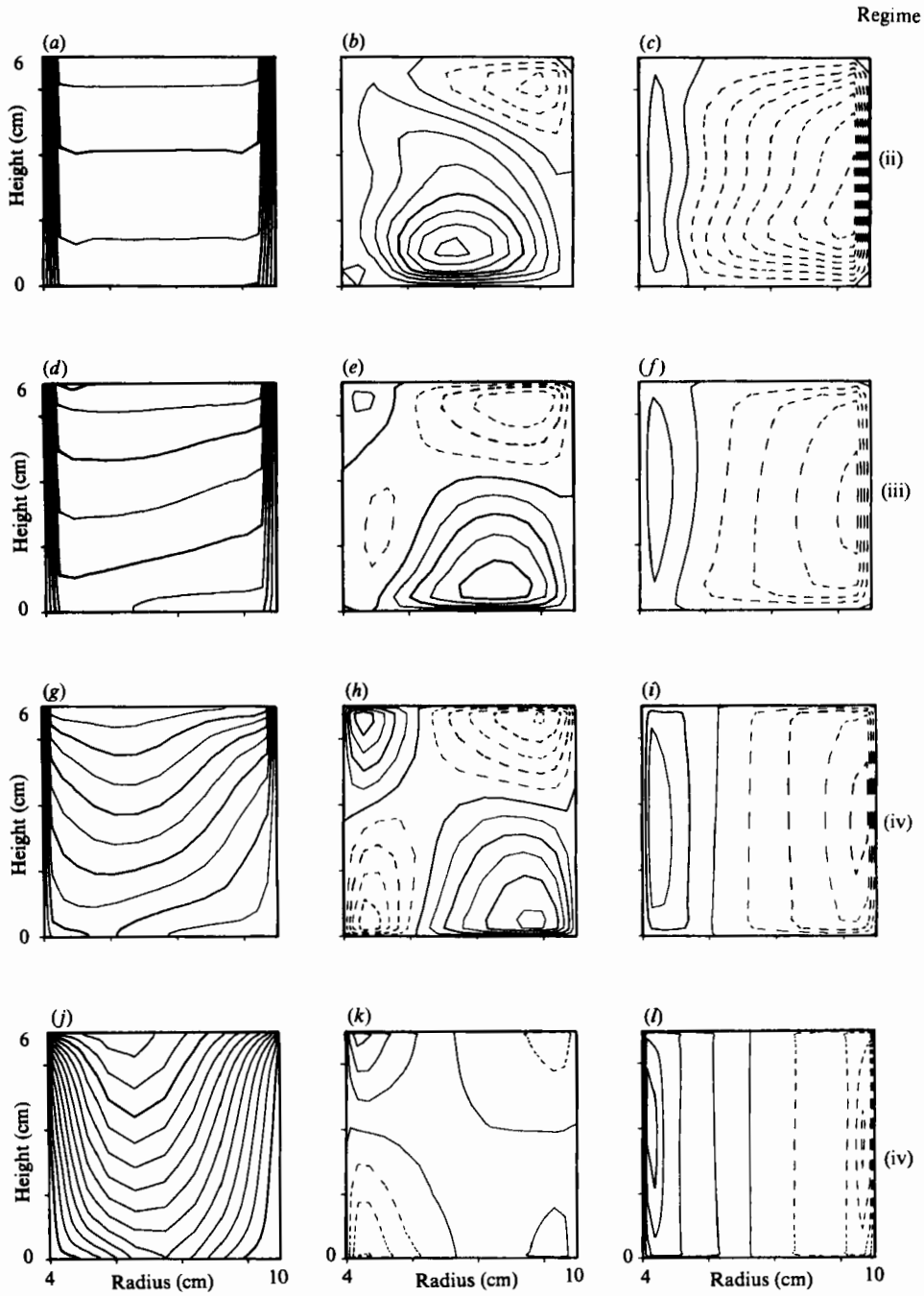

FIGURE 7. Contour maps of the temperature [(*a*), (*d*), (*g*) and (*j*)], azimuthal velocity [(*b*), (*e*), (*h*) and (*k*)] and meridional stream function ([(*c*), (*f*), (*i*) and (*l*)] fields, from numerical simulations of flow in an internally heated rotating annulus ($\epsilon = 1$) at values of $\mathcal{P}_n$ typical of axisymmetric regimes (ii)–(v). Fields correspond to regime (ii) [$\mathcal{P}_n = 5.8 \times 10^{-3}$; (*a*)–(*c*)], regime (iii) [$\mathcal{P}_n = 0.281$; (*d*)–(*f*)], regime (iv) [$\mathcal{P}_n = 1.26$; (*g*)–(*i*)] and regime (v) [$\mathcal{P}_n = 7.62$; (*j*)–(*l*)]. Contour intervals are 0.5 °C [(*a*), (*d*), (*g*)], 1.0 °C [(*j*)], 0.002 cm s^{-1} [(*b*)], 0.05 cm s^{-1} [(*c*) and (*h*)], 0.1 cm s^{-1} [(*k*)], 0.1 cm^2 s^{-1} [(*c*) and (*f*)], 0.05 cm s^{-1} [(*i*)] and 0.01 cm^2 s^{-1} [(*l*)]. All negative contours are dashed.

ψ-field indicates that the sidewall boundary layers asociated with u and w become steadily thinner as Ω increases. The latter result is consistent with the expected $E^{\frac{1}{3}}$ and $E^{\frac{1}{4}}$ dependence of the boundary layers of Stewartson-type (e.g. Fein 1978) applicable to the cylindrical annulus (cf. also figures 8–10 below).

4.6. *Dynamical balances*

Because the numerical model calculates an internally consistent set of temperature and motion fields for the flow to a degree of accuracy limited only by the numerical precision of the computer, it is straightforward to examine the spatial distribution of all the terms in the model equations (cf. Williams 1967*a*, *b*, 1972). As shown above, the model equations include analogues of the terms used in the scale analysis in §2, and we may therefore test the validity of the analysis directly by examining the detailed dynamical balances at every grid point in the flow.

Figure 8 shows a sequence of profiles of the terms in the thermodynamic equation as functions of r and z at mid-height and mid-radius respectively, for the axisymmetric flows illustrated in figure 7. All four radial profiles show a clear distinction between the sidewall boundary layers and the interior, with a vertical advection/diffusion balance predominating in the boundary layers in all cases (except, perhaps, in figure 8*g*). For regimes (ii), (iii) and (iv) (figure 8*a*, *c*, *e*), the diffusion term becomes very small in the interior, where the balance is largely between internal heating (with its r^{-2} radial dependence) and vertical advection (see §2.1 and 2.2). For the regime (v) example (figure 8*g*), however, the diffusion term has become comparable with vertical advection in the interior, because of the inhibiting effect of the Ekman layers on the meridional circulation. Horizontal advection hardly occurs in the sidewall boundary layers or the interior but is a dominant term in the Ekman layers. The vertical profiles in figure 8 illustrate the shrinking of the Ekman layers as P_n increases (whose thickness is indicated as E in figure 8*b*, *d*, *f*), and also show the important role of thermal diffusion in the Ekman layers, required to balance horizontal advection in regimes (iii)–(v) as the vertical advection term is forced towards zero by the impermeable boundary condition at $z = 0$ and d (see (4.3*b*)).

Similar profiles for the azimuthal momentum equation are shown in figure 9 for the same flows as above, but at $z = 0.2d$ and $r = a + 0.7(b-a)$ (since $v = 0$ at mid-height and mid-radius, and the corresponding profiles for this equation are not typical of the rest of the interior flow). For regimes (iii)–(v) (figure 9*c*–*h*), the dominant balance is largely between viscosity and the Coriolis term fu, with the advection term playing a subsidiary role except in the sidewall boundary layers (cf. §2.3). The balance in regime (ii) (figure 9*a*, *b*), however, appears to be more complicated in the interior, with the viscous term being relatively small. The implied approximate balance between the advective, Coriolis and metric (uv/r) terms is consistent with the near conservation of angular momentum m ($= r[\Omega r + v]$, cf. Williams 1967*a*; Read 1986*c*) suggested from the analysis of §2.3. The vertical section (figure 9*b*), however, shows the viscous term becoming large near the horizontal boundaries, largely balanced by the Coriolis term. This is apparently in conflict with the scale analysis of §2.3, though the Ekman number for this flow ($E = 4.17 \times 10^{-2}$) is a little larger than assumed in the scale analysis (the depth scale of the Ekman layer $h_E = 1.73$ cm, cf. the annulus depth $d = 6$ cm). The distinction between 'thin' Ekman layers and an interior flow is therefore only marginally valid. The profile does, however, indicate the presence of a secondary boundary-layer structure, in which the balance changes to one dominated by the viscous term, with a characteristic lengthscale $h_H < h_E$.

An estimate of h_H can be obtained by extending the scale analysis in §2, rescaling

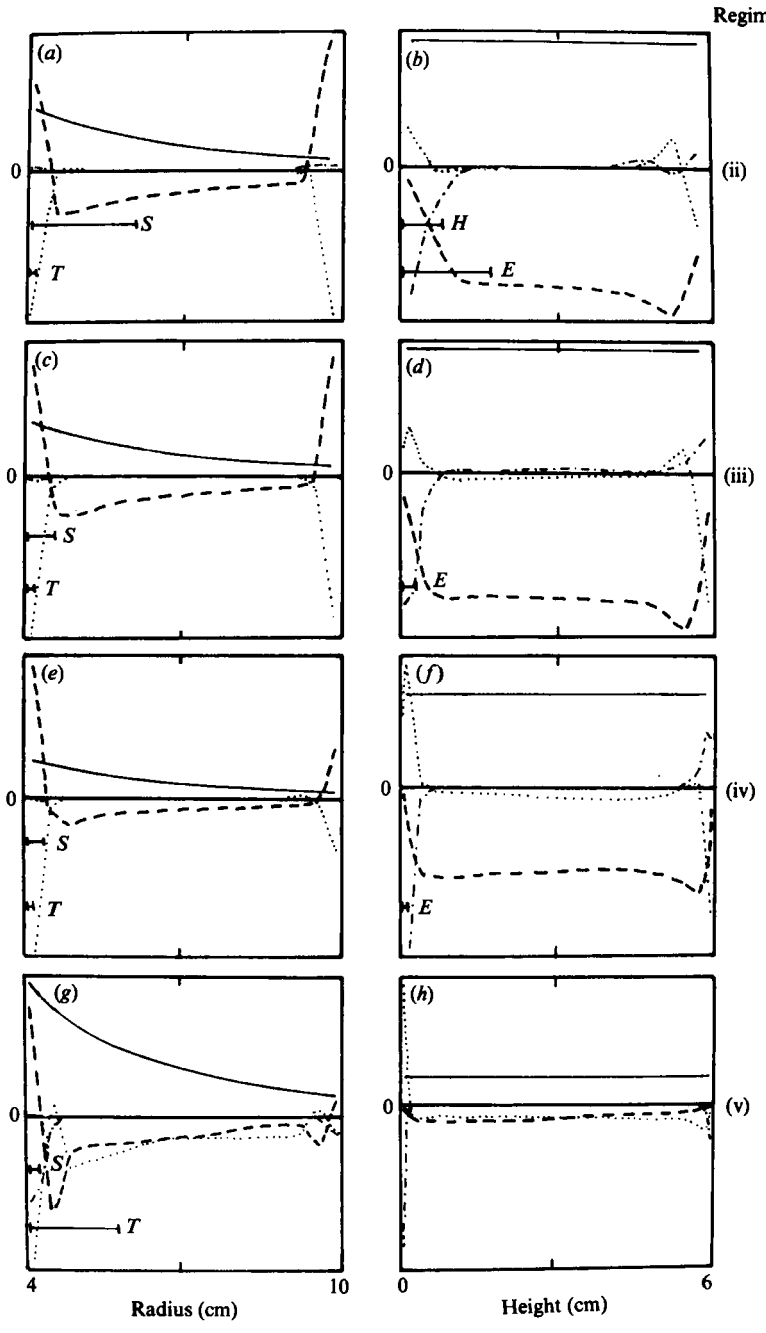

FIGURE 8. Profiles of the main terms in the thermodynamic equation (cf. (2.6)), obtained from the numerical simulations illustrated in figure 7 at values of P_n of 5.8×10^{-3} [(*a*), (*b*)], 0.281 [(*c*), (*d*)], 1.26 [(*e*), (*f*)] and 7.62 [(*g*), (*h*)]. Profiles are with respect to radius at mid-height [(*a*), (*c*), (*e*) and (*g*)], and with respect to height at mid-radius [(*b*), (*d*), (*f*) and (*h*)]. Terms plotted correspond to $q(r)$ (——); wT_z (– – –); uT_r (–·–·–); and $\kappa\nabla^2 T$ (·····). The thickness of the Ekman layer $(\nu/\Omega)^{\frac{1}{2}}$ is indicated as E in (*b*), (*d*) and (*f*), and that of the weak-rotation boundary layer (see text) as H in (*b*). The thicknesses of the sidewall thermal boundary layer and the $E^{\frac{1}{3}}$ Stewartson layer are indicated by T and S respectively in (*a*), (*c*), (*e*) and (*g*).

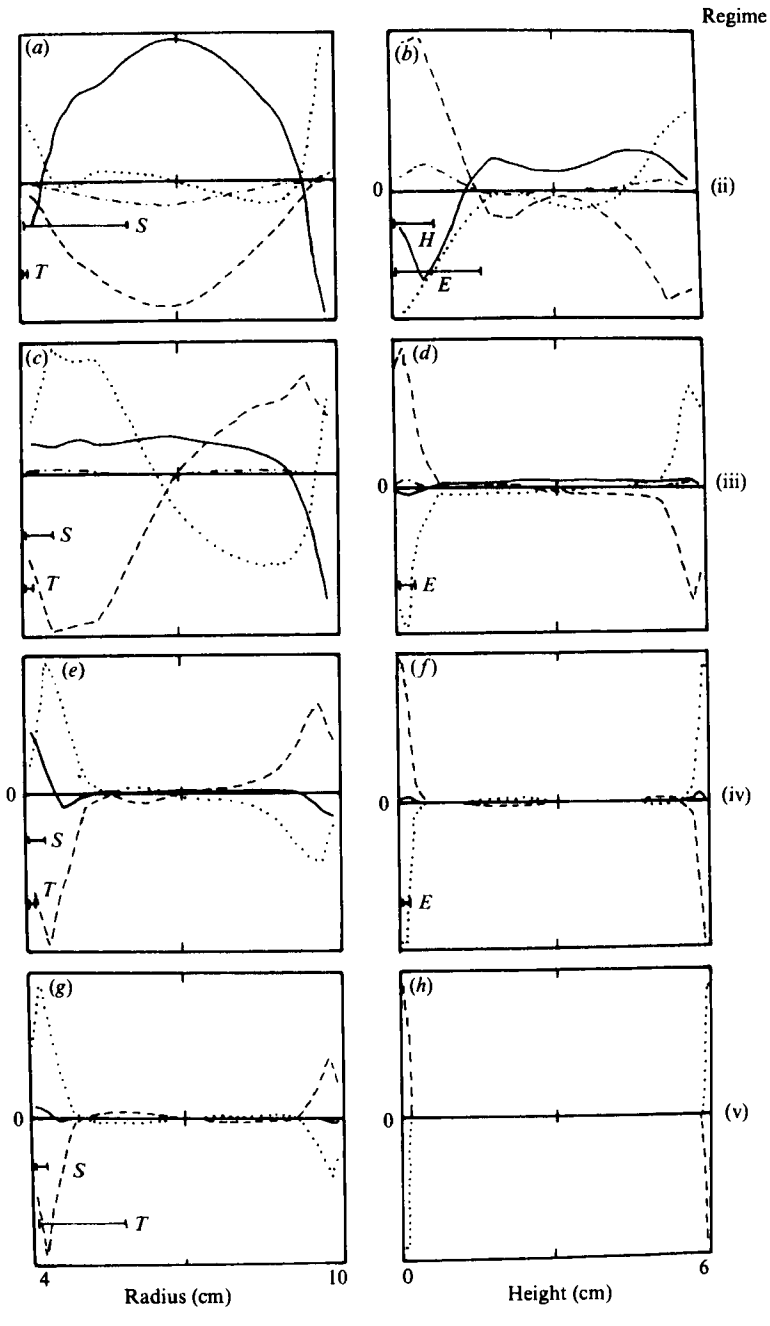

FIGURE 9. Profiles of the main terms in the azimuthal momentum equation (cf. (2.2)), obtained from the numerical simulations illustrated in figures 7 and 8. Profiles are with respect to radius at $z = 0.2d$ [(*a*), (*c*), (*e*) and (*g*)], and with respect to height at $r = a + 0.7(b-a)$ [(*b*), (*d*), (*f*) and (*h*)]. Terms plotted correspond to $-fu$ (– – –); $-\boldsymbol{u}\cdot\nabla v$ (——); $\nu(\nabla^2 v - v/r^2)$ (· · · · · ·); and $-uv/r$ (–·–·–). Boundary-layer lengthscales E, H, T and S are shown as for figure 8.

(2.2) using $\Delta z = h_H \Delta z_*$ (assuming $h_H \ll H$), $\Delta x = L\Delta x_*$, Ψ as given by (2.18) and $V = fL$ (see §2.3); thus

$$\nabla_*^2 v_* = \sigma^{-1}\epsilon^{\frac{3}{4}}A^{\frac{1}{4}}\frac{h_H}{L}\{(\psi_z)_* + J(v_*, \psi_*)\}. \tag{4.6}$$

For the viscous term to balance the Coriolis and advective terms in this boundary layer, we require

$$h_H = O(H\sigma\epsilon^{-\frac{1}{4}}A^{-\frac{1}{4}}), \tag{4.7}$$

which is, of course, independent of rotation rate. For the flow illustrated in figure 9(*a*, *b*), $h_H = 0.84$ cm (shown in figure 9*b* as H), and is seen to be a reasonably accurate measure of the size of the region of the flow dominated by the viscous term. It is significant that the limit $P = \epsilon^2\sigma^{-2}$ represents the case where $h_H = HE^{\frac{1}{4}} (= h_E)$, so that h_H is the thinnest horizontal boundary layer for the whole of region (ii). The arguments of §2.3 continue to apply in the derivation of the other main flow parameters, however, and the h_H boundary layer evidently acts as a passive layer, required to match v (and ψ) to the non-slip horizontal boundaries in the same way as the viscous sidewall boundary layers (where the balance of terms is similar).

Profiles for the azimuthal vorticity equation may be derived by taking the curl of the vertical and radial components of the momentum equation, and are shown in figure 10 for the same four examples as above. The profiles for regime (ii) (figure 10*a*, *b*) clearly confirm the buoyancy/viscous balance, anticipated from §2.3 and from the appearance of convective-overshoot patterns in §4.4, at most points in the flow, with some contribution from the advection term (present because σ is finite). In regimes (iii) and (iv) (figure 10*c*–*f*) the balance has completely changed over to being highly geostrophic (buoyancy/Coriolis) except in the boundary layers (although the Coriolis term remains a significant component of the vorticity balance in the sidewall boundary layers, especially near the outer sidewall). The horizontal boundary layers exhibit the Coriolis/viscous balance characteristic of a linear Ekman layer (see §2.3). For regime (v) (figure 10*g*, *h*), the balances remain dominated by the geostrophic terms but, to reach this regime with the geometry and heating rate used for other simulations in this series (preserving a constant value of A_c), a very rapid rotation rate (≈ 12 rad s^{-1}) was required. This renders the initial assumption that $\Omega^2 b \ll g$ for the scale analysis in §2 no longer strictly valid, so that the reduced centrifugal term $\Omega^2 r\alpha T_z$ becomes significant in the vorticity balance. The net result is that the interior flow becomes highly geostrophic with respect to the *apparent* vertical only, in the sense that the vorticity equation reduces to a thermal wind equation relating temperature gradients along a local *geopotential* surface to the shear of the azimuthal flow perpendicular to that surface.

5. Concluding remarks

We have presented a scheme of analysis for the axisymmetric flow in a fluid system heated internally and cooled at the side boundaries, which allows the classification of the flow according to a regime defined in terms of the dominant dynamical balances. From a consideration of the properties of each regime, the analysis enables the appropriate regime and its associated interdependence of flow parameters to be determined from the externally applied conditions (i.e. fluid properties, apparatus geometry, boundary conditions and heating and rotation rates). In common with several other comparable systems (e.g. HIK, Hignett 1982), the most significant dimensionles parameter is found to be the ratio ($P^{\frac{1}{4}}$) of the characteristic lengthscales

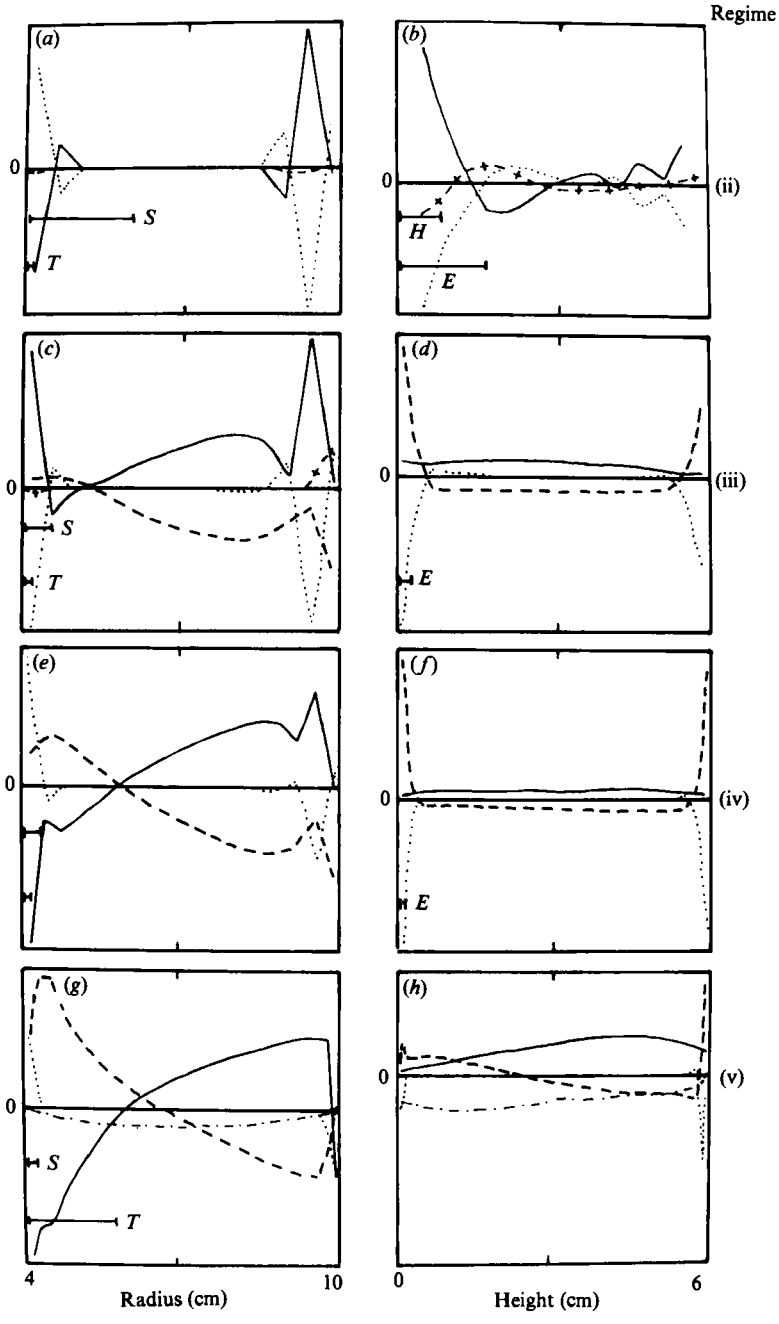

FIGURE 10. Profiles of the main terms in the azimuthal vorticity equation (cf. (2.4)), obtained from the numerical simulations illustrated in figures 7–9. Profiles are with respect to radius at mid-height [(*a*), (*c*), (*e*) and (*g*)], and with respect to height at mid-radius [(*b*), (*d*), (*f*) and (*h*)]. Terms plotted correspond to fv_z (– – – –); $-g\alpha T_r$ (——); $\nu(\nabla^2\zeta - \zeta/r^2)$ (· · · · · ·); $-\boldsymbol{u}\cdot\nabla\zeta + u\zeta/r^2$ (+ – + – + –); and $-\Omega^2 r\alpha T_z$ (·—·—·). Boundary-layer lengthscales E, H, T and S are shown as for figure 8.

associated with the non-rotating sidewall thermal boundary layer and the horizontal Ekman layer, a parameter which encapsulates a good deal of physical insight into the chief factors determining the nature of the flow. A complication in the present system is that $\mathcal{P}$ is an internal flow parameter, involving combinations of quantities such as ΔT, which are not under the direct control of an experimenter. By referring the system to the conduction-dominated state, however, using the parameter μ analogous to the Nusselt number of boundary-heated systems, we have shown how the flow can be determined from combinations of the externally imposed parameters while still retaining the physical insight offered by the use of a parameter related to $\mathcal{P}$.

Six main axisymmetric flow regimes have been identified, depending largely upon the value of $\mathcal{P}$ (and its external equivalent $\mathcal{P}_c$). Most of these regimes are characterized by rapid flow in the meridional plane in thin boundary layers adjacent to the horizontal and vertical boundaries, and weak vertical motion in a stably-stratified, advective interior driven by internal heating. While the Ekman layers remain much deeper than the thickness l_T of the diffusive thermal boundary layers, the meridional heat transport in the system is largely unaffected by rotation. As h_E begins to approach l_T, however, the rotational influence initially affects only the interior slope of the isotherms (while ΔT remains largely constant). When $h_E \lesssim l_T$, the Ekman layers dominate the meridional heat transport, gradually shutting off the advective component of heat transfer as h_E decreases. Eventually, the meridional flow is forced by the Ekman layers to be sufficiently weak that advection can no longer compete with diffusion, and the flow approaches the purely conductive state.

The analysis also indicates that the azimuthal flow in the interior is characterized by a geostrophic balance over a remarkably wide range of parameter space (requiring only that $\mathcal{P}$ exceed the small limit $\epsilon^2\sigma^{-2}$). A number of subtleties are encountered in determining the magnitude of V and its dependence on rotation, however, because the interior horizontal temperature contrast itself depends strongly upon rotation at low and moderate rotation rates. Only in the fully Ekman-dominated regimes (v) and (vi) is V given by the commonly assumed 'thermal-wind' scale, based on the total thermal contrast ΔT. At the lowest rotation rates, the Ekman layer plays no significant role in the flow, and the azimuthal flow matches onto the non-slip boundaries via passive viscous/advective boundary layers. The interior flow is then characterized largely by local conservation of angular momentum with a Rossby number $\mathcal{R} \approx 1$ (see table 1 and figure 1).

The conclusions of the scale analysis have also been extensively and quantitatively verified using both laboratory experiments (to measure the dependence of global parameters on $\mathcal{P}$) and numerical simulations. The latter have been shown to be particularly valuable in enabling the detailed balances in the basic equations to be studied, as well as the interdependence of the motion and temperature fields and their associated dimensionless parameters. The results of both studies have provided confirmation of the broad conclusions obtained from the scale analysis over a wide range of $\mathcal{P}_n$ and ϵ, at least within the limitations of the initial assumptions. The scheme of analysis in §2 may be seen, therefore, as providing a useful framework for the interpretation and intercomparison of results from different experimental configurations, in a similar way to the results of HIK and Hignett (1982), for the regimes accessible in actual experiments.

The occurrence of large-amplitude baroclinic waves for $\mathcal{P} \gtrsim 1$ in the laboratory provides striking confirmation of the assertion that such non-axisymmetric disturbances arise in order to assist in the azimuthally averaged advective heat transfer in

the meridional plane. Laboratory results from around the axisymmetric/wave transition suggest that, instead of decaying rapidly with Ω as $\mathcal{P}$ increases through unity, the wave-present value of μ remains close to the axisymmetric value measured at slightly lower values of $\mathcal{P}$. The role of baroclinic waves may therefore be regarded as replenishing the meridional transfer of heat towards that obtained in the absence of rotational constraints. By comparing the axisymmetric numerical simulations with measurements of the wave-present flows in the laboratory at similar points in parameter space, quantitative assessments of the effects of baroclinic waves can be obtained for comparison with theories of baroclinic-wave transports (e.g. Pfeffer & Barcilon 1978; Barcilon & Pfeffer 1979).

In connection with the latter, an important task is to define a suitable zonally symmetric state to use in studies of linear and weakly nonlinear baroclinic instability. The scale analysis in the present scheme identifies regime (iv) as that associated with the onset of baroclinic waves, so that any basic state invoked as the starting point for instability studies should be characterized by similar dynamical balances to those derived in §2.3. So far as the interior flow is concerned, the balances applicable to regime (iv) are similar to those usually assumed for many quasi-geostrophic analyses (e.g. Hide & Mason 1975; Pedlosky 1979; Gill 1982). This is found to be the case, even though a Rossby number based on the 'thermal-wind' scale for V (using ΔT rather than ΔT_{h}, and commonly referred to as the 'thermal Rossby number' $R_T (= R/\beta$ in regimes (iii) and (iv)), e.g. Hide & Mason 1975) may be only a little less than unity in many practical cases. Numerical simulations demonstrate, however, that the dominant dynamical balances for vorticity and zonal momentum are indisputably geostrophic for these cases, so that the quasi-geostrophic conditions under which Eady-type instability analyses may apply (e.g. Hide 1969; Hide & Mason 1975) are broadly satisfied for the interior. Appropriate boundary conditions are also of importance, though they have received little detailed attention in previous work. Studies based on the present approach can provide useful guidance concerning the type of boundary layers which are compatible with a given interior flow regime, e.g. for asymptotic analyses such as those of McIntyre (1968) for the boundary-heated annulus, HIK for the thermocline configuration, and Mobbs (1986) for the present system.

The latter considerations are clearly of interest in deciding the efficacy of a laboratory flow as a dynamical analogue of a geophysical system or feature. For the suggested analogy between the internally heated annulus flows and the cloud bands of Jupiter and Saturn (e.g. Read & Hide 1983, 1984; Read 1986*b*; also cf. Conrath & Pirraglia 1983), a quasi-geostrophic interior balance in the laboratory system is confirmed by the present work under conditions appropriate for baroclinic eddies. Such a regime is also believed to prevail in the Jovian atmosphere for lengthscales appropriate to the largest long-lived eddies (e.g. Stone 1976; Conrath *et al.* 1981; Mitchell *et al.* 1981; Read 1986*b*). The importance of diabatic heating needs to be carefully considered in the atmospheric context, however, especially with regard to the maintenance of the zonal wind structure, since it is clearly a dominant factor in the thermodynamic balance in the laboratory (and hence, perhaps, of importance in any potential vorticity budget, see Read 1986*a*, *b*).

HIK also discussed the use of their analysis (similar to that in §2 above) as directly applied to the large-scale circulation of the ocean. Although a parameter analogous to $\mathcal{P}$ could be defined for the oceans, the axisymmetric regimes derived were only of limited relevance to the real ocean because of three-dimensional effects (e.g. a closed-basin geometry) in the latter system. The possibility of applying the principles

of the analysis to an atmospheric context deserves further consideration, since three-dimensional effects due to large-scale topography may have a less extreme effect upon the circulation. An atmospheric system might then be more readily described in terms of a zonally symmetric system (as is frequently attempted in modelling studies, e.g. see Lorenz 1967; Charney 1973; Held & Hou 1980; Read 1986*d*). A careful consideration of the most significant boundary layers in an atmospheric model is clearly necessary, however, especially as an atmosphere does not usually invoke boundary layers as a means of heating and/or cooling, in contrast to most laboratory systems. The ensuing analysis could make use of more limited previous attempts at a scale analysis of axisymmetric or zonally averaged atmospheric models (e.g. Gierasch, Goody & Stone 1970; Stone 1972; Gierasch 1975), and thereby incorporate a greater degree of physical insight into the mechanisms of atmospheric circulation to supplement that afforded by the so-called 'similarity' approach (Golitsyn 1970).

In comparing the results of the scale analysis with the numerical simulations, examples have been presented in which discrepancies between the analytical and numerical results have indicated possible shortcomings in the operation of the model at the most rapid rotation rates with inadequate computational precision. Further uses of this combined analytical, laboratory and numerical approach may therefore include the important task of verifying and improving the formulation of numerical models for use in a wide variety of applications (cf. Hignett *et al.* 1985).

Thanks are due to Dr R. Hide for his continued interest and support, and especially to Drs P. Hignett and S. D. Mobbs for many fruitful discussions during the course of this work. The technical assistance of Mr W. D. N. Jackson and Mr I. M. Armstrong in carrying out the laboratory experiments, and Mr R. D. Carter and Ms H. M. Schrecker in programming the numerical model and some of the associated diagnostics, are gratefully acknowledged.

REFERENCES

ARAKAWA, A. 1966 Computational design for long term numerical integration of the equations of fluid motion. Two dimensional incompressible flow, Part 1. *J. Comp. Phys.* **1**, 119–143.

BARCILON, A. & PFEFFER, R. L. 1979 Further calculations of eddy heat fluxes and temperature variances in baroclinic waves using weakly non-linear theory. *Geophys. Astrophys. Fluid Dyn.* **12**, 45–60.

BOWDEN, M. & EDEN, J. F. 1965 Thermal convection in a rotating fluid annulus: temperature, heat flow and flow field observations in the upper symmetric regime. *J. Atmos. Sci.* **22**, 185–195.

CARRIGAN, C. R. 1985 Convection in an internally-heated, high Prandtl number fluid: a laboratory study. *Geophys. Astrophys. Fluid Dyn.* **32**, 1–22.

CHARNEY, J. G. 1973 Planetary fluid dynamics. In *Dynamic Meteorology* (ed. P. Morel), pp. 99–351. Reidel.

CONRATH, B. J., FLASAR, F. M., PIRRAGLIA, J. A., GIERASCH, P. J. & HUNT, G. E. 1981 Thermal structure and dynamics of the Jovian atmosphere 2. Visible cloud features. *J. Geophys. Res.* **86**, 8769–8775.

CONRATH, B. J. & PIRRAGLIA, J. A. 1983 Thermal structure of Saturn from Voyager infrared measurements: implications for atmospheric dynamics. *Icarus* **53**, 286–292.

ELDER, J. W. 1965 Laminar free convection in a vertical slot. *J. Fluid Mech.* **23**, 77–98.

FARNELL, L. 1980 Solution of Poisson equations on a non-uniform grid. *J. Comp. Phys.* **35**, 408–425.

FEIN, J. S. 1978 *Boundary Layers in Homogeneous and Stratified Fluids.* University Press of Florida.

FULTZ, D. 1961 Developments in controlled experiments on large-scale geophysical problems. *Adv. Geophys.* **7**, 1–103.

FULTZ, D., LONG, R. R., OWENS, G. V., BOHAN, W., KAYLOR, R. & WEIL, J. 1959 Studies of thermal convection in a rotating cylinder with some implications for large scale atmospheric motions. *Met. Monographs*, vol. 4, Am. Met. Soc.: Boston.

GIERASCH, P. J. 1975 Meridional circulation and the maintenance of the Venus atmospheric rotation. *J. Atmos. Sci.* **32**, 1038–1044.

GIERASCH, P., GOODY, R. & STONE, P. 1970 The energy balance of planetary atmospheres. *Geophys. Fluid Dyn.* **1**, 1–18.

GILL, A. E. 1966 The boundary-layer regime for convection in a rectangular cavity. *J. Fluid Mech.* **26**, 515–536.

GILL, A. E. 1982 *Atmosphere–Ocean Dynamics*. Academic.

GOLITSYN, G. S. 1970 A similarity approach to the general circulation of planetary atmospheres. *Icarus* **13**, 1–24.

HART, J. E. 1982 Finite amplitude baroclinic instability. *Ann. Rev. Fluid Mech.* **11**, 147–172.

HELD, I. M. & HOU, A. Y. 1980 Nonlinear axially symmetric circulation in a nearly inviscid atmosphere. *J. Atmos. Sci.* **37**, 515–533.

HIDE, R. 1953 Some experiments on thermal convection in a rotating liquid. Ph.D. thesis, Cambridge University.

HIDE, R. 1958 An experimental study of thermal convection in a rotating liquid. *Phil. Trans. R. Soc. Lond.* A **250**, 442–478.

HIDE, R. 1967*a* On the vertical stability of a rotating fluid subject to a horizontal temperature gradient. *J. Atmos. Sci.* **24**, 6–9.

HIDE, R. 1967*b* Theory of axisymmetric thermal convection in a rotating fluid annulus. *Phys. Fluids* **10**, 56–68.

HIDE, R. 1969 Some laboratory experiments on free thermal convection in a rotating fluid subject to a horizontal temperature gradient and their relation to the theory of the global atmospheric circulation. In *The Global Circulation of the Atmosphere* (ed. G. A. Corby), pp. 196–221, R. Met. Soc.: London.

HIDE, R. 1980 Jupiter and Saturn: giant, magnetic, rotating fluid planets. *Observatory* **100**, 182–193.

HIDE, R. 1981 High vorticity regions in rotating thermally-driven flows. *Met. Mag. Lond.* **110**, 335–344.

HIDE, R. & MASON, P. J. 1970 Baroclinic waves in a rotating fluid subject to internal heating. *Phil. Trans. R. Soc. Lond.* A **268**, 201–232.

HIDE, R. & MASON, P. J. 1975 Sloping convection in a rotating fluid. *Adv. Phys.* **24**, 47–100.

HIDE, R. & MASON, P. J. 1978 On the transition between axisymmetric and non-axisymmetric flow in a rotating annulus subject to a horizontal temperature gradient. *Geophys. Astrophys. Fluid Dyn.* **10**, 121–156.

HIGNETT, P. 1982 A note on the heat transfer by the axisymmetric thermal convection in a rotating fluid annulus. *Geophys. Astrophys. Fluid Dyn.* **19**, 293–299.

HIGNETT, P., IBBETSON, A. & KILLWORTH, P. D. 1981 On rotating thermal convection driven by non-uniform heating from below. *J. Fluid Mech.* **109**, 161–187.

HIGNETT, P., WHITE, A. A., CARTER, R. D., JACKSON, W. D. N. & SMALL, R. M. 1985 A comparison of laboratory measurements and numerical simulations of baroclinic wave flows in a rotating cylindrical annulus. *Q. J. R. Met. Soc.* **111**, 131–154.

JACKSON, W. D. N. 1984 A system for the real-time measurement of two-dimensional velocity fields. *Met. O. 21 Internal Rep.* IR/84/1. Available from the Meteorological Office Library, Bracknell, Berks.

JAMES, I. N., JONAS, P. R. & FARNELL, L. 1981 A combined laboratory and numerical study of fully-developed baroclinic waves in a cylindrical annulus. *Q. J. R. Met. Soc.* **107**, 51–77.

JONAS, P. R. 1980 Laboratory experiments and numerical calculations of baroclinic waves resulting from potential vorticity gradients at low Taylor number. *Geophys. Astrophys. Fluid Dyn.* **15**, 297–315.

JONAS, P. R. & KENT, P. M. 1979 Two-dimensional velocity measurement by automatic analysis of trace particle motion. *J. Phys.* E: *Sci. Instrum.* **12**, 604–609.

KAISER, J. A. C. 1971 Heat transfer by symmetrical rotating annulus convection. *J. Atmos. Sci.* **28**, 929–932.

LORENZ, E. 1967 *The nature and theory of the general circulation of the atmosphere.* World Meteorological Organisation No. 218, T.P.115.

MCINTYRE, M. E. 1968 The axisymmetric convective regime for a rigidly bounded rotating annulus. *J. Fluid Mech.* **32**, 625–655.

MASON, P. J. 1975 Baroclinic waves in a container with sloping endwalls. *Phil. Trans. R. Soc. Lond.* A **278**, 397–445.

MITCHELL, J. L., BEEBE, R. F., INGERSOLL, A. P. & GARNEAU, G. W. 1981 Flow fields within Jupiter's Great Red Spot and White Oval BC. *J. Geophys. Res.* **86**, 8751–8757.

MOBBS, S. D. 1986 The axisymmetric flow of an internally-heated, rotating fluid, in preparation.

PEDLOSKY, J. 1979 *Geophysical Fluid Dynamics.* Springer.

PFEFFER, R. L. & BARCILON, A. 1978 Determination of eddy fluxes of heat and eddy temperature variances using weakly non-linear theory. *J. Atmos. Sci.* **35**, 2099–2110.

PIACSEK, S. A. & WILLIAMS, G. P. 1970 Conservation properties of finite difference schemes. *J. Comp. Phys.* **6**, 392–405.

QUON, C. 1976 A mixed spectral and finite difference model to study baroclinic annulus waves. *J. Comp. Phys.* **20**, 442–479.

QUON, C. 1977 Axisymmetric states of an internally heated rotating annulus. *Tellus* **29**, 83–96.

READ, P. L. 1985 Finite-amplitude, neutral baroclinic eddies and mean flows in an internally-heated rotating fluid: 1. Numerical simulations and quasi-geostrophic "free modes". *Dyn. Atmos. Oceans* **9**, 135–207.

READ, P. L. 1986*a* Finite amplitude, neutral baroclinic eddies and mean flows in an internally-heated rotating fluid: 2. Effects of spatially-varying static stability. *Dyn. Atmos. Oceans* (submitted).

READ, P. L. 1986*b* Stable, baroclinic eddies on Jupiter and Saturn: a laboratory analogue and some observational tests. *Icarus* (in press).

READ, P. L. 1986*c* Super-rotation and diffusion of axial angular momentum: I. "Speed limits" for axisymmetric flow in a rotating cylindrical fluid annulus. *Q. J. R. Met. Soc.* **112**, 231–251.

READ, P. L. 1986*d* Super-rotation and diffusion of axial angular momentum: II. A review of quasi-axisymmetric models of planetary atmospheres. *Q. J. R. Met. Soc.* **112**, 253–272.

READ, P. L. & HIDE, R. 1983 Long-lived eddies in the laboratory and in the atmospheres of Jupiter and Saturn. *Nature* **302**, 126–129.

READ, P. L. & HIDE, R. 1984 An isolated barocolinic eddy as a laboratory analogue of the Great Red Spot on Jupiter? *Nature* **308**, 45–49.

STONE, P. H. 1972 A simplified radiative–dynamical model for the static stability of rotating atmospheres. *J. Atmos. Sci.* **29**, 405–418.

STONE, P. H. 1976 The meteorology of the Jovian atmosphere. In *Jupiter: Studies of the Interior, Atmosphere, Magnetosphere and Satellites* (ed. T. Gehrels). University of Arizona Press, Tucson. pp. 586–618.

UKAJI, K. 1979 Thermal and dynamical structures of convective motions in a rotating fluid annulus subject to internal heating. *J. Met. Soc. Japan* **57**, 532–547.

WHITE, A. A. 1986 Steady, finite amplitude Rossby waves and mean flows – analytical illustrations of the Charney–Drazin non-accleration theorem. *Q. J. R. Met. Soc.* (in press).

WILLIAMS, G. P. 1967*a* Thermal convection in a rotating fluid annulus: Part I. The basic axisymmetric flow. *J. Atmos. Sci.* **24**, 144–161.

WILLIAMS, G. P. 1967*b* Thermal convection in a rotating fluid annulus: Part II. Classes of axisymmetric flow. *J. Atmos. Sci.* **24**, 162–174.

WILLIAMS, G. P. 1969 Numerical integration of the three-dimensional Navier–Stokes equations for incompressible flow. *J. Fluid Mech.* **37**, 727–750.

WILLIAMS, G. P. 1972 The field distributions and balances in a baroclinic annulus wave. *Mon. Wea. Rev.* **100**, 29–41.